Elucidating the local structure of $Li_{1+x}Al_xTi_{2-x}(PO_4)_3$ and $Li_3Al_xTi_{2-x}(PO_4)_3$ (x = 0, 0.3) *via* total scattering

Matthew S. Chambers,*[a] Jue Liu,[b] Olaf J, Borkiewicz,[c] Kevin Llopart[a], Robert L Sacci[a] ,Gabriel M. Veith*[a]

[a]Chemical Sciences Division, Oak Ridge National Laboratory, Oak Ridge, Tennessee 37831, United States

[b] Neutron Scattering Division, Oak Ridge National Laboratory, Oak Ridge, Tennessee 37831, United States

[c] X-ray Science Division, Advanced Photon Source, Argonne National Laboratory, Lemont, Illinois 60439, United States

ORCiD:

1. Matthew Chambers – 0000-0002-7893-9603
2. Jue Liu – 0000-0002-4453-910X
3. Olaf J. Borkiewicz – 0000-0003-2370-3393
4. Kevin Llopart – 0009-0009-4969-7957
5. Robert Sacci – 0000-0002-0073-5221
6. Gabriel Veith – 0000-0002-5186-4461

*Corresponding author

Corresponding authors' e-mail addresses:

chambersms1@ornl.gov (Matthew S. Chambers), veithgm@ornl.gov (Gabriel M. Veith)

Abstract

$Li_{1+x}Al_xTi_{2-x}(PO_4)_3$ (LATP) and $Li_3Al_xTi_{2-x}(PO_4)_3$ (x = 0, 0.3) are promising candidates in all-solid-state batteries due to their high room temperature conductivity of 10^{-3} S cm^{-1} and air- and moisture-stability. They also exhibit unusual thermal expansion properties, with $Li_{1+x}Al_xTi_{2-x}(PO_4)_3$ showing near-zero thermal expansion along the a axis while $Li_3Al_xTi_{2-x}(PO_4)_3$ exhibits polynomial positive thermal expansion along the a axis and polynomial negative thermal expansion along the c axis. A crucial component to

understanding these properties is understanding the local structure. Total scattering is a powerful analytical technique as it provides information on the long-range, average structure as well as the local structure. Here, we report the first X-ray and neutron total scattering experiments performed on $Li_{1+x}Al_xTi_{2-x}(PO_4)_3$ and $Li_3Al_xTi_{2-x}(PO_4)_3$ (x = 0, 0.3). We show that the PO_4 and TiO_6 polyhedra experience very little expansion of the P/Ti–O bonds up to 800 °C, nor is there much expansion when the Li content increases significantly. The minor thermal expansion of the nearest-neighbor bonds of the polyhedra is revealed to be the reason behind the unusual thermal expansion properties, causing the near-zero thermal expansion along *a* in $Li_{1+x}Al_xTi_{2-x}(PO_4)_3$ and moving as whole units in $Li_3Al_xTi_{2-x}(PO_4)_3$. The structural robustness of the framework is also the reason for the increased conductivity as Li content increases, as the framework remains undistorted as Li content increases, permitting Li-ion mobility as the number of charge carriers increases. This suggests that phosphate-based framework materials beyond LATP would also be a good material space to explore for new Li-ion (and other ion-) conducting materials.

Introduction

In recent years, there has been a global push to achieve net-zero carbon emissions. A critical technology to achieve this goal is lithium-ion batteries (LIBs). Commercial LIBs typically use an electrolyte that consists of a lithium salt, such as $LiPF_6$, dissolved in an organic liquid, *e.g.* ethylene carbonate.[1] While liquid electrolytes can achieve a conductivity of 10^{-2} – 10^{-1} S cm^{-1}, other issues arise from them such as flammability,[2] the small transference number[1, 3] and the formation of Li dendrites when used with a Li metal anode.[2, 3] One solution to these problems is to use an inorganic, solid-state electrolyte instead of the liquid electrolyte.[1-4] $Li_{1+x}Al_xTi_{2-x}(PO_4)_3$ is one such candidate,[5-8] as it is air- and moisture-stable[9] as well having a high ionic conductivity.[10] Although $LiTi_2(PO_4)_3$ was first discovered as an ionic conductor with a conductivity of 1×10^{-6} S cm^{-1} by Zu-xiang *et al.*,[11] $Li_{1+x}Al_xTi_{2-x}(PO_4)_3$ was first found to be a good Li-ion conductor by Aono *et al.*,[12] who found that the x = 0.3 sample achieved a conductivity of 7×10^{-4} S cm^{-1} at 298 K and later[13] reporting a bulk conductivity of 10^{-3} S cm^{-1} compared to the bulk conductivity of $LiTi_2(PO_4)_3$ of 1×10^{-4} S cm^{-1}. On the other hand, Arbi *et al.*[14] have reported a bulk conductivity of 4.8 ±

0.5×10^{-3} S cm^{-1} for $Li_{1.3}Al_{0.3}Ti_{1.7}(PO_4)_3$. Impedance spectroscopy performed on single crystals found that the $x = 0.3$ sample achieves a conductivity of 5.14×10^{-3} S cm^{-1} at room temperature while the $x = 0.4$ sample achieved a similar conductivity of 5.67×10^{-3} S cm^{-3} at the same temperature.[15] Aliovalent doping has also been done with Sc^{3+}, Y^{3+}, La^{3+} and Ga^{3+},[16-19] Ca^{2+}, Mg^{2+} and Sr^{2+},[8] and Nb^{5+},[20] while isovalent doping has been done with Ge^{4+},[10, 21-24] Zr^{4+},[8, 25] Sn^{4+},[26] Si^{4+},[13] and Hf^{4+}.[8, 18] There has also been anion-doping using F^-,[7, 27] and S^{2-}.[28] $LiTi_2(PO_4)_3$ adopts the NASICON structure,[21] (Figure 1) named after $NaZr_2(PO_4)_3$ (**Na** Super **I**onic **Con**ductor) discovered by Goodenough *et al.*,[29] which adopts the *R*-3*c* space group and consists of a framework of PO_4 tetrahedra corner-connected to TiO_6 at every vertex.

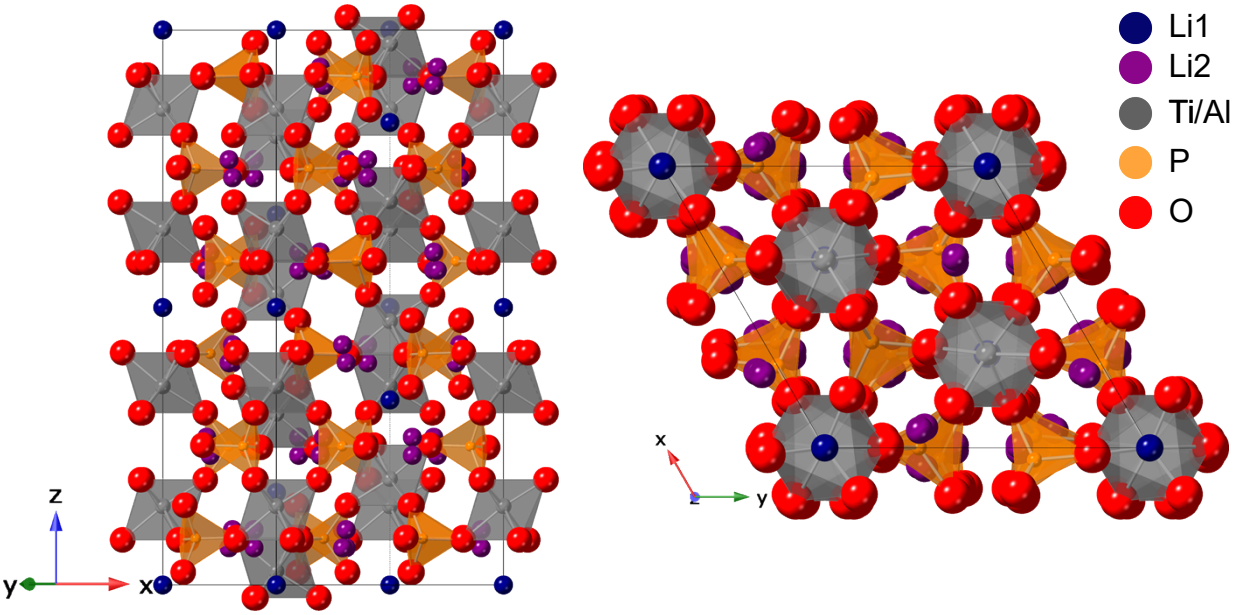

Figure 1 – Crystal structure of $Li_{1+x}Al_xTi_{2-x}(PO_4)_3$

The Li^+ cations are situated on the so-called M1 site at (0, 0, 0) (Wyckoff position: 6*b*), which positions them at the unit cell corners and edges as well as within cavities of the $Ti_2P_3O_{12}$ framework. As the tetravalent cation is substituted by trivalent cations, additional Li^+ ions occupy the interstitial M2 site [(1/12, 1/3, 1/12)],[30-32] located between PO_4 polyhedra, and are said to facilitate the fast Li-ion conduction. $Li_{0.9}Ti_{1.9}Nb_{0.1}(PO_4)_3$, which utilizes Nb^{5+} substitution to create Li^+ vacancies, resulted in a lower conductivity of 3.2×10^{-8} S cm^{-1} at 300 K compared to 5.8×10^{-7} S cm^{-1} found for $LiTi_2(PO_4)_3$ at the same

temperature.[20] However, ^{93}Nb NMR suggests that Nb atoms may be occupying some M2 sites, acting as a further block for Li^+ conduction. Furthermore, $Li_{1+x}Al_xTi_{2-x}(PO_4)_3$ can be fully lithiated with *n*-butyl lithium in hexane, producing $Li_3Al_xTi_{2-x}(PO_4)_3$ by reducing the Ti^{4+} cations to Ti^{3+}.[30, 31, 33, 34] The lithiation is accompanied by a loss of the mirror plane perpendicular to the *c* axis, resulting in the adoption of the *R*-3 space group. Furthermore, the M1 site is completely unoccupied, instead resulting in Li^+ ions being located at the M2, M3 and M3' sites,[30, 31] where the M3 sites are also located near (1/12, 1/3, 1/12). In the *R*-3*c* space group, M3 and M3' sites are symmetrically equivalent, but the loss of the *c* glide plane in the *R*-3 space group leads to them becoming independent sites. Despite the symmetry lowering, Zhang *et al*.[30] reported that $Li_3Ti_2(PO_4)_3$ had a higher room-temperature conductivity of 1.9×10^{-4} S cm^{-1} compared to 1.01×10^{-5} S cm^{-1} for $LiTi_2(PO_4)_3$. They attribute the increased ionic conductivity to two primary reasons: (i) the Li^+ ions being located on the M2 and M3 sites and the diffusion bottleneck in $Li_3Ti_2(PO_4)_3$ being larger than the bottleneck in $LiTi_2(PO_4)_3$. Despite the fact that the fully lithiated $Li_3Ti_2(PO_4)_3$ is reported to have a higher conductivity, the optimum value of x in $Li_{1+x}Al_xTi_{2-x}(PO_4)_3$ is thought to be $x \leq 0.3$, attributed to the formation of $Li_4P_2O_7$ and $AlPO_4$ secondary phases,[32] but $x = 0.4$ has been reported as the optimum substitution limit.[15] Furthermore, Arbi *et al*.[34] reported Li^+ mobility to be larger in $Li_3Al_{0.2}Ti_{1.8}(PO_4)_3$ than in $Li_3Ti_2(PO_4)_3$. On the other hand, $Li_3Sc_2(PO_4)_3$ adopts a monoclinic structure (space group: $P2_1/n$) at room temperature and undergoes a phase transition to orthorhombic (space group: *Pbcn*) at 300 °C,[19] which may be due to the difference in ionic radii of sixfold Sc^{3+} (0.745 Å) and sixfold Ti^{3+} (0.67 Å).[35]

Additionally, NASICON structures have unusual thermal expansion properties. Woodcock and Lightfoot[36] found that $LiTi_2(PO_4)_3$ has a near-zero thermal expansion coefficient (TEC) for the *a* axis ($\alpha_a = 0.748 - 0.272 \times 10^{-6}$ K^{-1} from 20 – 800 °C), while the *c* axis exhibits a linear TEC of $\alpha_c = 30.8 \times 10^{-6}$ K^{-1} from 20 – 800 °C, resulting in a volumetric TEC of $\alpha_V = 25.7 - 37.7 \times 10^{-6}$ K^{-1} in the same temperature range. They attribute this unusual thermal expansion to the movement of Li^+ cations from M1 to M2 sites. On the other hand, Zhang *et al*.[30] reported positive thermal expansion along both *a* and *c* for $LiTi_2(PO_4)_3$, with a volumetric TEC of $\alpha_V = 30 \times 10^{-6}$ K^{-1}. $NaTi_2(PO_4)_3$ and $KTi_2(PO_4)_3$ also experienced anisotropy with their

TECs,[36] although to lesser degrees (α_a = –5.3 × 10^{-6} K^{-1}, α_c = 20.8 × 10^{-6} K^{-1} and α_a = –0.13 × 10^{-6} K^{-1}, α_c = 6.62 × 10^{-6} K^{-1} respectively). They also attribute these expansion properties due to the occupation of the M2 sites; the large K^+ in $KTi_2(PO_4)_3$ causing smaller expansion due to the increased distortion of the PO_4 tetrahedra already present at room temperature. On the other hand, Arbi *et al*.[31] reported that $Li_3Al_xTi_{2-x}(PO_4)_3$ (x = 0, 0.3) adopt polynomial positive thermal expansion (PTE) along the *a* axis and a polynomial negative thermal expansion (NTE) along the *c* axis, with mean expansion coefficients of 1.4 × 10^{-4} Å K^{-1} for x = 0 and 1.7 × 10^{-4} Å K^{-1} for x = 0.3, while Zhang *et al*.[30] reported that the x = 0 sample exhibits PTE for the *a* cell and NTE for the *c* cell (making no comment on whether it is linear or polynomial), with an overall volumetric expansion of α_V = 20 × 10^{-6} K^{-1}. However, $Sr_{0.5}Ti_2(PO_4)_3$, which also adopts the *R*-3 space group, exhibits a near zero TEC along *c* α_c = –0.02 × 10^{-6} K^{-1}, while the *a* cell exhibited a TEC of α_a = 13.2 × 10^{-6} K^{-1}.[37] This thermal expansion behavior is attributed to the fact that there is ordering of Sr^{2+} and vacancies, where the Sr^{2+} sites expand along the *c* axis as the vacancy sites contract. A follow up study by the same group[38] on $La_{0.33}Ti_2(PO_4)_3$ confirmed that the M1 occupancy is critical to the unusual expansion, as $La_{0.33}Ti_2(PO_4)_3$ had TECs of α_a = 12.44 × 10^{-6} K^{-1} and α_c = –1.53 K^{-1}. Recently, the thermal expansion properties of $Bi_{0.33}Zr_2(PO_4)_3$ (space group: *P*3*c*1) have been studied, where there is NTE along both *a* (α_a = –12.99 × 10^{-6} K^{-1}) and *c* (α_c = –26.67 × 10^{-6} K^{-1}), contrary to most NASICON materials.[39] These unique thermal expansion properties may be beneficial to forming all-solid-state batteries through heating or other bonding approaches.

It is clear from the literature that $Li_{1+x}Al_xTi_{2-x}(PO_4)_3$ and $Li_3Al_xTi_{2-x}(PO_4)_3$ (x = 0, 0.3) have a rich structural chemistry. It is therefore critical to understand both the local and long-range structure in order to further understand the conduction mechanism. Although solid-state NMR (ssNMR) studies have been performed previously,[14, 31, 32, 34] to date, there have been no studies on these materials using total scattering. Total scattering is a technique that uses both the diffuse scattering and Bragg diffraction in order to determine the long-range and short-range structure simultaneously.[40, 41] Upon applying a sine Fourier transform to the total scattering function, the pair distribution function (PDF) can be produced, which can be used to examine

the differences in short-range structure between $Li_{1+x}Al_xTi_{2-x}(PO_4)_3$ and $Li_3Al_xTi_{2-x}(PO_4)_3$, as well as further understand the unusual thermal expansion properties. We have therefore collected both variable-temperature (VT) X-ray and room temperature neutron total scattering data on that $Li_{1+x}Al_xTi_{2-x}(PO_4)_3$ and $Li_3Al_xTi_{2-x}(PO_4)_3$ (x = 0, 0.3) samples and performed modelling against the neutron PDF data using least-squares refinements with a single unit cell,[42] analogous to Rietveld refinement to elucidate their short-range structures, *i.e*. "small box modelling" or "small box refinement". In addition, we have collected *in-situ* X-ray total scattering data for the sol-gel synthesis of $LiTi_2(PO_4)_3$, as diffuse scattering is present in amorphous samples, providing some insights into this alternative synthesis route.

Experimental

Solid state synthesis of $Li_{1+x}Al_xTi_{2-x}(PO_4)_3$ (x = 0, 0.3)

Stoichiometric amounts of TiO_2 (Strem, 99%), Al_2O_3 (Aesar, 99%) and $NH_4H_2PO_4$ (Sigma, 99.5%) and 10 wt% excess Li_2CO_3 (Aesar, 99%) were mixed in a 125 ml HDPE Nalgene® bottle with ~70 ml 0.5" diameter yttria-stabilized zirconia cylinders and isopropanol on a roller mill for 44 h. The moist powder was extracted, ground in a porcelain mortar and pestle and dried for 1 – 2 h in aluminum dishes at 100 °C in a furnace. The powder was then heated at 350 °C, during which the $NH_4H_2PO_4$ decomposes, releasing NH_3. Due to the molar proportion (and thus mass) of $NH_4H_2PO_4$ in this reaction, the sample would melt at this stage. The sample was extracted and ground using a porcelain mortar and pestle. The ground powder was then pressed into a 2" diameter pellet using 20 drops of 1:20 weight percent Duramax:H_2O solution. The pellet was heated at 450 °C for 2 h to remove the Duramax and H_2O, immediately followed by heating to 950 °C for 6 h. The white pellets were ground using a mortar and pestle, followed by a Spex® mill with 5/32" stainless steel media for 2 × 10 min with 2 min rests before powder patterns were collected and used in the lithiation syntheses described below. This synthesis results in ~20 g of sample, with a target of 25 g.

To obtain electrochemical impedance spectroscopy measurements, 5 g of sample were made by griding stoichiometric amounts of TiO_2 (Strem, 99%), Al_2O_3 (Aesar, 99%) and $NH_4H_2PO_4$ (Sigma, 99.5%) and 10

wt% excess Li_2CO_3 (Aesar, 99%) in an agate mortar and pestle, followed by heating the sample at 300 °C (10 °C min^{-1} heating rate) for 2 h in an Al dish. The sample was extracted and ground in an agate mortar and pestle and heated at 950 °C for 6 h (10 °C min^{-1}).

Synthesis of $Li_3Al_xTi_{2-x}(PO_4)_3$ (x = 0, 0.3)

$Li_3Al_xTi_{2-x}(PO_4)_3$ (x = 0, 0.3) were synthesized by lithiating ~2 g of $Li_{1+x}Al_xTi_{2-x}(PO_4)_3$ samples described above. The samples were dried at 80 °C for 24 h, then under vacuum in an Ar-filled glove box antechamber at ambient temperatures for 24 h before being transferred to the inside. 10 ml of 2.5M *n*-butyllithium in hexane solution (Sigma) were added to each sample in glass conical flasks and the samples were left stirring for 1 month using rubber stoppers to prevent evaporation of hexane. Upon addition of the *n*-butyl lithium, the samples immediately changed color from white to grey/lavender. The samples were extracted through Büchner funnel filtration in the glove box, washing the samples thoroughly with hexane. The samples were further dried in a vacuum oven outside the glove box at 60 °C for 21 h on the filter paper, then ground with an alumina mortar and pestle, resulting in fine, lavender-colored powders (Figure S1a).

For conductivity measurements, the synthesis was repeated using ~0.8 g of the of $Li_{1+x}Al_xTi_{2-x}(PO_4)$ (x = 0, 0.3) from the original 20 g batches and ~2 g of $Li_{1+x}Al_xTi_{2-x}(PO_4)_3$ from the 5 g batches prepared for conductivity measurements. Following the procedure reported by Zhang *et al*.,[30] who reported synthesizing $Li_3Ti_2(PO_4)_3$ after only 2 days of lithiation of $LiTi_2(PO_4)_3$, the 0.8 g batches were left stirring in 5 ml 2.5 M *n*-butyl lithium (Sigma) for 12 days and the ~2 g batches were left for 13 days. The samples were filtered as above but dried at 80 °C in an oven in air on the filter paper for 30 minutes, then ground with an agate mortar and pestle after drying.

Safety:* n-*butyl lithium is pyrophoric. When disposing of it, it can be treated by adding isopropanol to form lithium isopropoxide as a precipitate. Isopropanol must be added dropwise as this reaction is exothermic.

Sol-gel synthesis of $LiTi_2(PO_4)_3$

Sol-gel synthesis was performed by adapting the process outlined by Ma *et al*.[43] 5 ml of HNO_3 (Aldrich, 70 wt%) was mixed with 15 ml deionized water. 7.333 g of $Ti(iOPr)_4$ (Acros, 98%) was added to the HNO_3 solution dropwise under stirring, producing some white precipitate. 11.2609 g of citric acid (Aldrich, 99.5%) was added to the mixture and the sample was heated to 60 °C, forming a yellow solution and dissolving most of the white precipitate. ***Care must be taken with heating at this stage as NO_x gases can be emitted***. 0.8896 g $LiNO_3$ was added to the hot stirring solution. At this point, all traces of precipitate were no longer present. 4.4513 g $NH_4H_2PO_4$ (Aldrich, 99.5%) was added to the sol/solution, forming a gel. The gel was dried at 80 °C in a muffle furnace for approximately 24 h. The dried gel was ground with a mortar and pestle, heated to 700 °C for 4 h, ground and then heated to 800 °C for 4 h producing a white powder. Heating and cooling rates were 10 °C min^{-1} in all heating steps inside of the muffle furnace. This synthesis targets 5 g of product.

For the *in-situ* X-ray total scattering study, the above steps were repeated up to drying the gel. After the gel was dried, the sample was heated to 300 °C for 6 h to remove any organic solvents and the gel framework, producing a black powder.

Laboratory powder X-ray diffraction

Powder X-ray diffraction (XRD) was performed using a Rigaku SmartLab with a HyPix detector to determine phase purity. A 2:1 mixture of Cu $K\alpha_1$:$K\alpha_2$ (λ_1 = 1.54056 Å, λ_2 = 1.54439 Å) was employed in Bragg-Brentano geometry with a range of $10 \leq \theta/2\theta \leq 90°$ and a scan rate of 1.5° min^{-1}. Data were collected using stationary bulk glass sa'mple holders.

X-ray total scattering

X-ray total scattering data were collected at 11-ID-B beamline at the Advanced Photon Source (APS) using monochromatic radiation with a wavelength of λ = 0.2116 Å. Samples were loaded into open-ended quartz

capillaries with a diameter of 1 mm. Quartz wool was inserted into the capillaries to seal and ensure a tight packing of the sample. Two samples were loaded into one capillary, separated with quartz wool. The capillaries were placed between resistive heating elements assembled by wrapping Kanthal wires around alumina tubes, as described previously.[44] Thermocouples were inserted into the capillaries to control the temperature of the sample. A Python script provided by the APS was used to adjust the temperature and collect data based on the readings of the thermocouple, which also controls the resistive heating elements. This setup is shown in Figure S2. Data were collected at 25 °C, then 100 – 800 °C in 50 °C increments, except for on the sol-gel samples, which were collected from 300 – 800 °C in 100 °C increments, at heating rates of 10 °C min^{-1}. Samples were allowed to equilibrate for 1 minute after reaching the specified temperature before measurements were made. Scans were collected for 10 minutes at 30 and 800 °C and 7.5 minutes at all other temperatures. Data were also collected on empty sample holders for total scattering processing.

Data were reduced from the raw images using GSASII,[45] processing to a maximum of $2\theta = 46°$ and using a NIST CeO_2 674b standard as the calibration image. A mask was applied to remove the beam stop from the image. The reduced data were used in Rietveld refinements.

Total scattering data were produced using GudrunX v5[46] and the reduced data from above. Data were processed using a $Q_{max} = 18$ $Å^{-1}$ with a Lorch correction[47] function of 0.01 Å, resulting in PDF using the $D(r)$ function as defined by Keen.[41] Data at $r < 1.0$ were Fourier filtered. Scattering from the empty capillary at each temperature was subtracted from the data during processing. In order to process the reduced data, an in-house Python script was used to reformat the files so that they could be read by GudrunX.

Neutron total scattering

Neutron total scattering was performed on the NOMAD beamline at the Spallation Neutron Source (SNS). Samples were loaded into quartz capillaries with a diameter of 3 mm and sealed with a lid. Time-of-flight (TOF) data were collected using five detector banks at the following center angles: $2\theta = 15°$ (bank 1), $2\theta =$

31° (bank 2), 2θ = 67° (bank 3), 2θ = 144° (bank 4) and 2θ = 154° (bank 5). During data collection, the capillaries were spun. The data were reduced for Rietveld refinement using IDL software.[48]

PDF data were produced using Addie software, producing the reduced $G(r)$ with a Q_{max} = 35 Å^{-1}. Background scattering from the empty capillary was subtracted using data collected on an empty capillary. Normalization was carried out against scattering signal from a 6 mm V rod. Data at the low r part (≤ 1.0 Å) were back Fourier filtered to reduce the effect from large noise in the high-Q scattering data.

Rietveld refinement

Rietveld refinements[49] were performed against laboratory XRD data, synchrotron XRD data and neutron XRD data using TOPAS Academic v7.[50] Structures were derived from the following starting models: $LiTi_2(PO_4)_3$ (Redhammer *et al*.[51]), $Li_{1.3}Al_{0.3}Ti_{1.7}(PO_4)_3$ (Pogosova *et al*.[52]), $Li_3Ti_2(PO_4)_3$ (Aatiq *et al*.)[33] and $Li_3Al_{0.22}Ti_{1.78}(PO_4)_3$ (Arbi *et al*.).[31]

Refinements against laboratory XRD data were performed in order to determine phase purity. The background was modelled using a 12th-order Chebyshev polynomial and the peak shapes were modelled using a Thompson-Cox-Hastings pseudo-Voigt function. The cell parameters were permitted to refine with symmetry constraints. A single isotropic atomic displacement parameter (ADP) was used. For the solid-state synthesized $Li_{1+x}Al_xTi_{2-x}(PO_4)_3$ (x = 0, 0.3) samples, preferred orientation was modelled using an eight-fold spherical harmonic function.

Rietveld refinements were performed against Bragg data obtained from X-ray total scattering experiments in order to obtain cell parameters. In addition to using 12th-order Chebyshev polynomial to model the background, the data collected for the empty quartz capillary were included to model the background. Peak shapes were again modelled using a pseudo-Vogit function. Cell parameters were allowed to refine with symmetry constraints. Atomic site coordinates were refined with symmetry constraints, in addition to giving each site its own ADP, but site occupancies were not refined. Initial refinements were performed against

data collected at 30 °C for each sample, then parametric refinements[53] were performed for the variable temperature (VT) analysis.

Rietveld refinements were performed against TOF neutron data. Initial refinements were performed using bank 5 only, but banks 2-4 were also included in subsequent refinements, including the final refinements. Instrumental calibration constants and contributions to peak shapes were determined using a NIST 640e Si standard and were fixed during refinement. Backgrounds were modelled using 12th-order Chebyshev polynomials and peak shapes were modelled using pseudo-Voigt functions for each bank. Cell parameters (with symmetry constraints), atomic site coordinates, and isotropic ADPs were allowed to refine. Li occupancies and Al/Ti occupancies were also permitted to refine in certain refinements, described in more detail below. Additionally, peak shape broadening due to sample crystallite sizes was modelled using a pseudo-Voigt function.[54]

PDF small box refinement

PDF small box refinements were performed using TOPAS Academic v7.[42] For neutron PDF analysis, starting models obtained from the Rietveld refinements were used, with the long-range space group symmetry (*R*-3*c* for $Li_{1+x}Al_xTi_{2-x}(PO_4)_3$, *R*-3 for $Li_3Al_xTi_{2-x}(PO_4)_3$). Additionally, ISODISTORT[55, 56] was used to produce symmetry-lowered structures (*R*-3 and *P*3*c*1 for $Li_{1+x}Al_xTi_{2-x}(PO_4)_3$, *R*3 and *P*-3 for $Li_3Al_xTi_{2-x}(PO_4)_3$). These space groups were selected as they are maximal subgroups of the parent symmetries. *R*3 symmetry was not used for $Li_{1+x}Al_xTi_{2-x}(PO_4)_3$ as it results in more unique atomic sites per unit cell than *P*3*c*1, and *P*3*c*1 provided an adequate fit (see the Results and Discussion below). Cell parameters and atomic site coordinates were allowed to refine. Additionally, thermal parameters were modelled using BeqPDFFit and beq_rcut_rlo_spherical (details can be found in the supplementary materials).

Electrochemical impedance spectroscopy (EIS)

EIS data were collected using a Biologic SP 200 potentiostat at a temperature of 23 °C, and a 1/2in diameter stainless-steel PEEK cells with two electrodes, with one working and one counter. The leads for the drive and sense lines were shorted just before the PEEK to minimize the impact of the setup impedance. For $Li_{1+x}Al_xTi_{2-x}(PO_4)_3$ samples, ~0.6 g of sample were pressed into 13 mm diameter pellets using 74 MPa of pressure and sintered at 950 °C for 6 h. Additionally, as a dense pellet was not produced for $LiTi_2(PO_4)_3$, pellets of $Li_{1+x}Al_xTi_{2-x}(PO_4)_3$ with the same dimensions were sintered at 1200 °C for 2 h, as reported By Zhang *et al*.[30] Approximately 845 Å of Au was sputtered under Ar onto both sides of the pellets in order to provide good electrical contact. The spectra were collected with a frequency range of 100 mHz to 7 MHz. For $Li_3Al_xTi_{2-x}(PO_4)_3$, ~0.5 g of sample were pressed into 13 mm diameter pellets using 74 MPa of pressure and sintered at 800 °C and 925 °C under flowing Ar for 2 h. However, the samples decomposed under these sintering temperatures (see discussion below for more details). Therefore, ~0.1 g of sample were loaded into the PEEK cell with a constant applied pressure of 39 MPa. Pellet thicknesses could not be determined as they broke upon ejection of the cell The impedance data were fit to a two-time constant blocking circuit, whereby the time constants were composed by two parallel resistor and capacitor sets in series along with an external capacitor. The lattice conductivity was taken from the high-frequency semicircle with a capacitance of 10^{-10} – 10^{-9} F and the grain boundary was taken from the low-frequency semicircle with a capacitance of ~10^{-6} F.

Results and discussion

Two samples of $Li_{1+x}Al_xTi_{2-x}(PO_4)_3$ (x =0, 0.3) were synthesized with traditional solid-state synthesis in order to study the effect Li-doping has on the local structure. These samples were also fully lithiated to form $Li_3Al_xTi_{2-x}(PO_4)_3$ (x = 0, 0.3) as these are the most that sample can be lithiated and thus represent the most that the structure can be distorted by Li^+ ions. Additionally, $LiTi_2(PO_4)_3$ was synthesized *via* the sol-gel method so that the evolution of the local structure could be investigated *in-situ* and the two synthesis techniques could be compared.

X-ray diffraction and total scattering

Laboratory X-ray diffraction

Laboratory X-ray diffraction was used to confirm that the desired phases had been successfully synthesized. The Rietveld plots for the solid-state synthesized materials are shown in Figure S3. In all samples, there are some unaccounted peaks at $2\theta \approx 18.6°$ and 27.1°. In the patterns of $LiTi_2(PO_4)_3$ (Figure S3a) and $Li_{1.3}Al_{0.3}Ti_{1.7}(PO_4)_3$ (Figure S3b), there are also small peaks visible at $2\theta \approx 29.1$ and 36.0°. These peaks are less visible in the patterns of $Li_3Ti_2(PO_4)_3$ (Figure S3c) and $Li_3Al_{0.3}Ti_{1.7}(PO_4)_3$ (Figure S3d), although the peaks in the range of $26.8 \leq 2\theta \leq 28.1°$ are more prominent in the pattern of $Li_3Al_{0.3}Ti_{1.7}(PO_4)_3$. We estimate these impurities to be no more than 1 weight % of the total product. As $Li_{1+x}Al_xTi_{2-x}(PO_4)_3$ (x = 0, 0.3) materials were used to synthesize $Li_3Al_xTi_{2-x}(PO_4)_3$ materials, the unaccounted peaks likely arise from the same phase. In the refinement of $LiTi_2(PO_4)_3$, the (2 0 –4) reflection shows a difference in intensity between the calculated and observed patterns, which is due to preferred orientation. This was likely caused by the sample mounting since this difference is not evident in the synchrotron and neutron data, which were collected in capillaries. The lithiation syntheses were repeated in order to attempt the measure the conductivity (see discussion below). The Rietveld plots for these additional syntheses are given in Figure S4 and are in excellent agreement with those shown in Figure S3c and Figure S3d, indicating that the synthesis is repeatable and that lithiation can be completed in 12 days. Figure S5 shows the Rietveld plot and diffraction patterns of the sol-gel-synthesized materials. When heated to 800 °C, $LiTi_2(PO_4)_3$ was formed (Figure S5a), with the impurity peaks that were present in the solid-state synthesis being far less prominent. Figure S5b shows the sol-gel synthesis only heated to 300 °C, indicating that the sample is amorphous. The broad peak at ~26° could correspond to amorphous sp^2 (*i.e.* graphite-like) carbon.[57]

Synchrotron total scattering – diffraction

Rietveld refinements were also performed against synchrotron Bragg data.

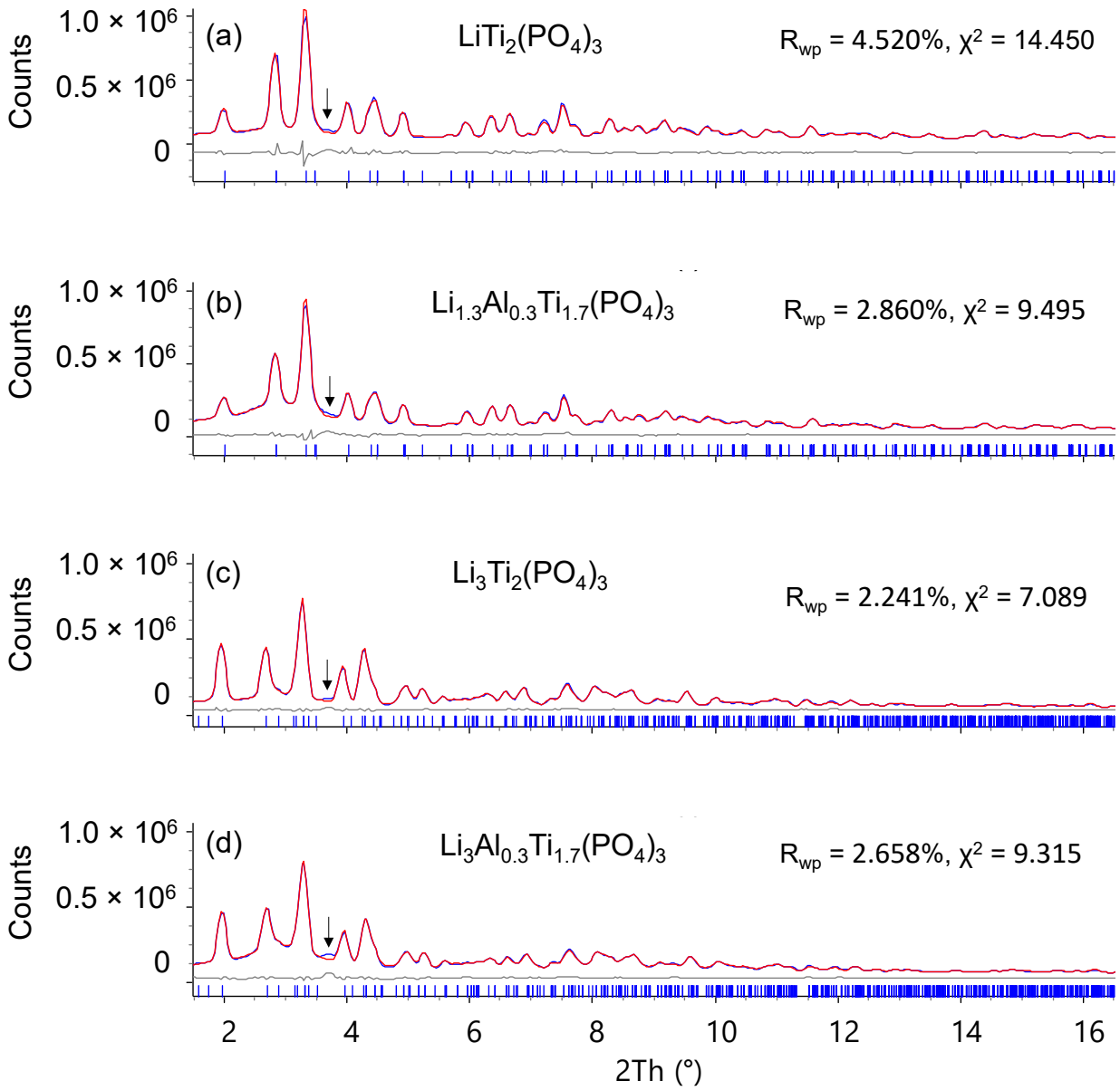

Figure 2 – Rietveld plots for $Li_{1+x}Al_xTi_{2-x}(PO_4)_3$ and $Li_3Al_xTi_{2-x}(PO_4)_3$ (x = 0, 0.3) obtained from X-ray total scattering measurements (λ = 0.2116 Å). (a) $LiTi_2(PO_4)_3$; (b) $Li_{1.3}Al_{0.3}Ti_{1.7}(PO_4)_3$; (c) $Li_3Ti_2(PO_4)_3$; (d) $Li_3Al_{0.3}Ti_{1.7}(PO_4)_3$. Blue curves = observed data; red curves = calculated patterns; grey curves = difference between observed and calculated. Blue tick marks correspond to reflections arising from $Li_{1+x}Al_xTi_{2-x}(PO_4)_3$ and $Li_3Al_xTi_{2-x}(PO_4)_3$ (x = 0, 0.3); black arrows correspond to unaccounted peaks.

The unaccounted peak at $2\theta \approx 3.7°$ corresponds to the unaccounted peak seen in the laboratory X-ray data at $2\theta \approx 27.1°$ ($Q \approx 1.9$ Å^{-1}), while the other unaccounted peaks are not visible due to the instrument resolution. The Rietveld refinements for the sol-gel syntheses (Figure S6) are very similar those seen in Figure 2 and Figure S3. Figure S6a shows the *ex-situ* sol-gel pattern, while Figure S6b shows the *in-situ* sol-gel synthesis pre-heating. Before heating, the majority of the pattern is derived from the quartz capillary, resulting in an "excellent" fit when the empty capillary is used as a background function (shown in the variable-temperature (VT) refinements). At 700°C, Bragg reflections arising from $LiTi_2(PO_4)_3$ become visible and dominate the pattern (Figure S6c). This is maintained after being heated to 800 °C (Figure S6d) and upon cooling; the room temperature pattern (Figure S6e) is very similar to the *ex-situ* pattern as expected. Due to the small quantity of solid heated during this experiment, the unaccounted peak seen at $2\theta \approx 3.7°$ is very small in the post-heating *ex-situ* sample.

*Thermal evolution of $Li_{1+x}Al_xTi_{2-x}(PO_4)_3$ and $Li_3Al_xTi_{2-x}(PO_4)_3$ (*x = 0, 0.3)*

After initial room-temperature refinements were performed, VT, parametric refinements[53] were performed in to investigate the thermal evolution of the cell parameters in the solid-state syntheses, which are shown in Figure 3.

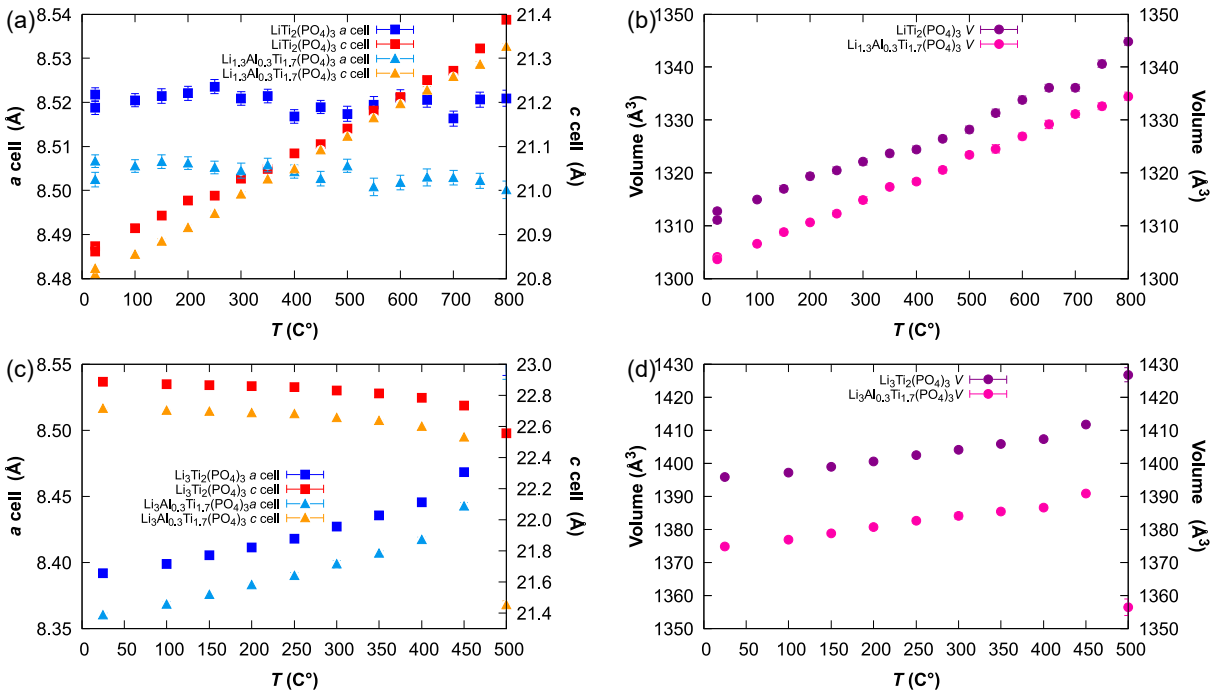

Figure 3 – Thermal evolution of the cell parameters from X-ray total scattering of: (a) $Li_{1+x}Al_xTi_{2-x}(PO_4)_3$ (x = 0, 0.3) a and c cells; (b) $Li_{1+x}Al_xTi_{2-x}(PO_4)_3$ (x = 0, 0.3) cell volumes; (c) $Li_3Al_xTi_{2-x}(PO_4)_3$ (x = 0, 0.3) a and c cell parameters; (d) $Li_3Al_xTi_{2-x}(PO_4)_3$ (x = 0, 0.3) cell volumes. $Li_3Al_xTi_{2-x}(PO_4)_3$ (x = 0, 0.3) samples begin to decompose at T = 500 °C, so their cell parameters are only plotted to 500 °C.

It can be seen that the a cell parameters for both $LiTi_2(PO_4)_3$ and $Li_{1.3}Al_{0.3}Ti_{1.7}(PO_4)_3$ (Figure 3a) exhibit a near-zero thermal expansion. The a cell parameters in Figure 3a have estimated standard deviations (σ) of approximately 0.002 Å. Due to this level of precision, TECs for the a cells over the entire temperature range cannot be determined, however we can use the equation $\frac{\Delta L}{L_0} = \alpha \Delta T$, where α = TEC, for the a cell parameters at 298.15 K (L_0) and 1073.15 K (L, $\Delta L = L - L_0$). For $LiTi_2(PO_4)_3$, α_a = –0.1(4) × 10^{-6} K^{-1}, and for $Li_{1.3}Ti_{1.7}(PO_4)_3$, α_a = –1.0(4) × 10^{-6} K^{-1}. The difference in the a cell parameters absolute value is due to the substitution of Al^{3+} on Ti^{4+} sites. On the other hand, the c cell parameters exhibit a near-linear thermal expansion, with TECs in the temperature range of 25 – 800 °C of α_c = 30.3 × 10^{-6} K^{-1} and α_c = 32.5 × 10^{-6} K^{-1} for $LiTi_2(PO_4)_3$ and $Li_{1.3}Al_{0.3}Ti_{1.7}(PO_4)_3$ respectively, with approximately linear volumetric expansions of α_V = 29.5 × 10^{-6} K^{-1} and 30.7 × 10^{-6} K^{-1}. As there is very little thermal expansion along the a axis, the

volumetric TEC has a similar magnitude to the TEC along *c*. These values are in good agreement with the values obtained for $LiTi_2(PO_4)_3$ by Woodcock and Lightfoot,[36] who found values of $\alpha_a = 0.748 - 0.272 \times 10^{-6}$ K^{-1}, $\alpha_c = 30.8 \times 10^{-6}$ K^{-1} and $\alpha_V = 25.7 - 37.7 \times 10^{-6}$ K^{-1} from 20 – 800 °C. They are also in good agreement with the volumetric TEC reported by Zhang *et al*.[30] of $\alpha_V = 30 \times 10^{-6}$ K^{-1}. The near-zero thermal expansion of $Li_{1+x}Al_xTi_{2-x}(PO_4)_3$ has implications for their implementation into solid-state batteries; the sample will be expanding along the *c* axis only, so the orientation of the grains needs to be considered during processing or if the cells are operated in varying temperatures. $Li_{1+x}Al_xTi_{2-x}(PO_4)_3$ could also be mixed with a material that experiences negative thermal expansion along one or more of its crystallographic axes, creating a composite material with zero thermal expansion.

The thermal evolution of the cell parameters of $Li_3Ti_2(PO_4)_3$ and $Li_3Al_{0.3}Ti_{1.7}(PO_4)_3$ are shown in Figure 3c and Figure 3d. Instead of exhibiting near-zero thermal expansion, the *a* cells both undergo a polynomial positive thermal expansion, while the *c* cells undergo a polynomial negative thermal expansion, resulting in an overall positive volumetric thermal expansion. This was similarly reported by Arbi *et al*.[31] While these materials possess non-linear TECs, approximate linear thermal expansion coefficients can be determined through a linear least-squares fit. The approximate linear TECs for $Li_3Ti_2(PO_4)_3$ are $\alpha_a = 19.9 \times 10^{-6}$ K^{-1}, $\alpha_c = -14.2 \times 10^{-6}$ K^{-1} and $\alpha_V = 25.5 \times 10^{-6}$ K^{-1}, while the linear TECs for $Li_3Al_{0.3}Ti_{1.7}(PO_4)_3$ are $\alpha_a = 21.3 \times 10^{-6}$ K^{-1}, $\alpha_c = -16.9 \times 10^{-6}$ K^{-1} and $\alpha_V = 25.7 \times 10^{-6}$ K^{-1}. The temperature range for these TECs is 25 – 450 °C. The volumetric TECs obtained here are similar in value to the one obtained for $Li_3Ti_2(PO_4)_3$ by Zhang *et al*.,[30] who reported a TEC of $\alpha_V = 20 \times 10^{-6}$ K^{-1}. That the TECs are so similar in $Li_3Al_xTi_{2-x}(PO_4)_3$ indicates that doping Al^{3+} onto Ti^{3+} sites has not affected the mechanism of thermal expansion. At $T \geq 500$ °C, the $Li_3Al_xTi_{2-x}(PO_4)_3$ (x = 0, 0.3) samples began to decompose, likely due to the oxidation of Ti^{3+} to Ti^{4+}. Positive thermal expansion for the *a* cell parameter and negative thermal expansion for the *c* cell parameter were reported in $Li_3Ti_2(PO_4)_3$ by Zhang *et al*.,[30] who obtained a volumetric TEC of $\alpha_V = 20 \times 10^{-6}$ K^{-1}. Woodcock and Lightfoot[36] suggested that the shrinking of the *a* cell of $LiTi_2(PO_4)_3$ is due to migration of the Li^+ ions from the M1 site to the M2 sites, which is supported by the different thermal expansion

properties exhibited by $La_{0.33}Ti_2(PO_4)_3$[38] as there is no migration of the M cations, and $Li_3Ti_2(PO_4)_3$, both in the study by Zhang *et al.*[30] and in this study, where Li ions do not occupy the M1 site, instead occupying M3 and M3'.

Variable temperature (VT) X-ray PDF

In order to further elucidate the mechanism behind the unusual thermal expansion properties, VT-total scattering was employed. Figure 4 shows the PDFs obtained for $Li_{1+x}Al_xTi_{2-x}(PO_4)_3$ and $Li_3Al_xTi_{2-x}(PO_4)_3$ (x = 0, 0.3) at 25 °C, 800 °C ($Li_{1+x}Al_xTi_{2-x}(PO_4)_3$) and 450 °C ($Li_3Al_xTi_{2-x}(PO_4)_3$).

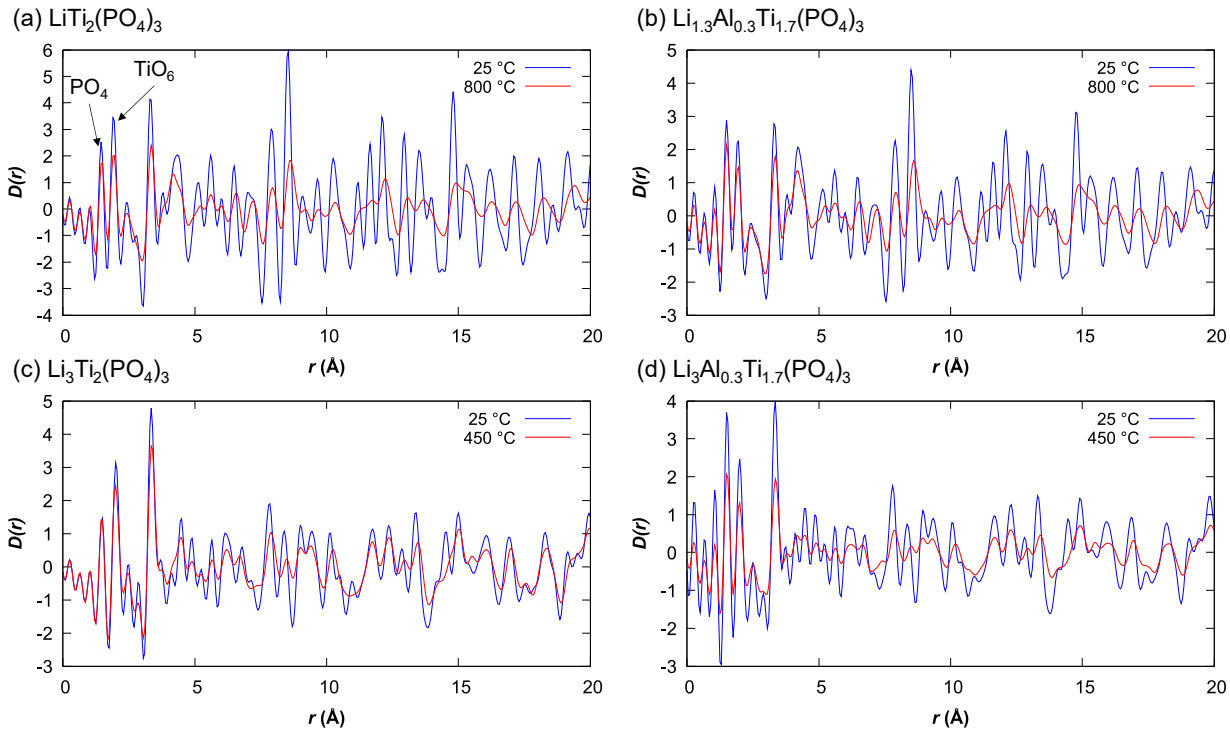

Figure 4 – Experimental X-ray PDFs (Q_{max} = 18 Å^{-1}) at selected temperatures of (a) $LiTi_2(PO_4)_3$.; (b) $Li_{1.3}Al_{0.3}Ti_{1.7}(PO_4)_3$; (c) $Li_3Ti_2(PO_4)_3$ and (d) $Li_3Al_{0.3}Ti_{1.7}(PO_4)_3$.

In all samples, there is a remarkable lack of change to the first two peaks at $r \approx 1.55$ Å, corresponding to the nearest-neighbor P–O bonds in the PO_4 tetrahedra and $r \approx 1.90$ [Figure 4(a–b)] and $r \approx 2.0$ Å [Figure 4(c–d)], corresponding to the nearest neighbor Ti–O bonds. This reveals the nature of the low PTE exhibited in the $Li_{1+x}Al_xTi_{2-x}(PO_4)_3$ (x = 0, 0.3) materials: the $Ti_2(PO_4)_3$ framework is structurally robust, showing <

0.02 Å change in the P–O nearest neighbor peak from 25 °C to 800 °C. This small change in P–O bond lengths has been observed in the long-range structure previously, although it is thought that there is still rotation and distortions within the tetrahedra.[36] In addition to the small change in the P–O nearest neighbor distance, there is also little change even in the O–O nearest neighbor distances ($r \approx 3.3$ Å). This structurally robust framework experiences little expansion, forcing the unit cell to expand along the *c* axis, likely also facilitated by the movement of Li^+ ions from M1 to M2 sites as suggested by Lightfoot and Woodcock.[38] Furthermore, this is an unusual property of thermal expansion. Typically, in framework materials that experience NTE, locally bonds increase with temperature due to the nature of the Morse potential, where NTE is a long-range phenomenon caused by cations moving closer to each other, such as with Zr–O–Zr in ZrW_2O_8, decreasing the Zr—Zr distance resulting in a shrinking of the unit cell,[58] or Zn–CN–Zn in $Zn(CN)_2$.[59] However, in the case of $Li_{1+x}Al_xTi_{2-x}(PO_4)_3$, the low thermal expansion also occurs locally. This intriguing result highlights the importance of applying total scattering to functional materials, as it can elucidate phenomena that Bragg scattering alone cannot. Despite there also being a lack of change to the first distances in the $Li_3Al_xTi_{2-x}(PO_4)_3$ materials, they do exhibit modest thermal expansion ($\alpha_V = 25.5 \times 10^{-6}$ K^{-1} for $x = 0$ and $\alpha_V = 25.7 \times 10^{-6}$ K^{-1} for $x = 0.3$). This indicates that as the material is heated, the polyhedral units move further away from each other along the *a* axis, which in turn causes the *c* axis to shrink, as the nearest neighbor distances are not significantly changing but the unit cell parameters do, indicating that locally there is little change to the bond distances in the polyhedra. The thermal expansion is similar to a wine rack, which shrinks along one set of axes as it is stretched out. This is likely caused by the movement of Li^+ ions from the M2 sites to M3 sites and vice versa. Furthermore, this indicates that the framework is robust enough to locally be unperturbed by the large amount of Li ions, which may explain why the room-temperature conductivity of $Li_3Ti_2(PO_4)_3$ ($\sigma = 1.9 \times 10^{-4}$ S cm^{-1}) is larger than that of $LiTi_2(PO_4)_3$ (1.01×10^{-5} S cm^{-1}).[30] The similarity between the P–O distances across all of the samples also indicates that the PO_4 tetrahedra are robust enough to accommodate additional Li^+ charge carriers without locally distorting, facilitating the increase in conductivity. Additionally, a ^{31}P ssNMR experiment also

showed very little change in the P environments from 100 to 500 K.[31] This point is discussed more below with the neutron total scattering results.

Sol-gel X-ray total scattering

In-situ X-ray total scattering was performed to study the evolution of the sol-gel synthesis of $LiTi_2(PO_4)_3$. An *ex-situ*, VT-total scattering experiment was also performed as a comparison to the solid-state method and the *in-situ* experiment. Figure 5 shows the X-ray PDFs of the *in-situ* synthesis.

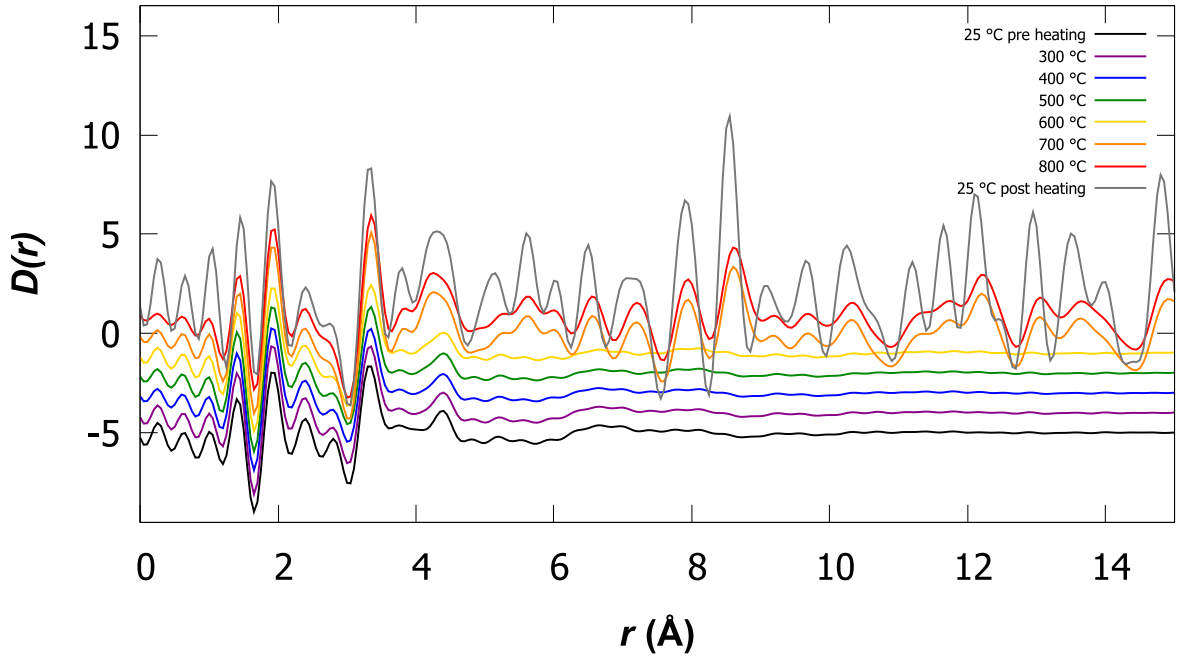

Figure 5 – *In-situ* sol-gel X-ray PDFs of $LiTi_2(PO_4)_3$

It can be seen that at the start of the experiment, the sample has very short-range order, showing very weak correlations at $r > 6$ Å and no correlations at $r \geq 10$ Å. The amorphous nature of the starting material was clear from the laboratory X-ray data (Figure S5b) and the lack of Bragg peaks in the first *in-situ* scan (Figure S6b). The sample remains highly amorphous until 700 °C, where the long-range order increases, showing correlations up to $r = 50$ Å (Figure S7a) and Bragg peaks first become visible (Figure S6c). This long-range order is maintained at 800 °C and post heating (Figure 5). Intriguingly, the peaks at $r < 5$ Å are very similar

throughout the entire temperature range, indicating that the NASICON framework has already locally formed through the sol-gel synthesis after heating to 300 °C, and that the additional temperatures cause the sample to crystallize (as well as remove any remaining carbon from the organic components). There are two very distinct peaks in the amorphous materials at $T < 700$ °C at $r \approx 2.4$ Å and 2.8 Å, which are broader at $T = 700$ and 800 °C, as well as the post-heated sample. These peaks correspond to the Li–O, O–O and Ti–Li distances, indicating that there is slightly more order in the amorphous samples with these distances. The peaks from $3.3 \leq r \leq 4.6$ Å also become broader after crystallization, indicating that the crystalline NASICON material has a broader distribution of O–O distances than the amorphous precursor. After heating, the PDF of the *in-situ* samples is very similar to the *ex-situ* sol-gel sample, as well as the sample synthesized through the solid-state method (Figure S7b). This indicates the *in-situ* synthesis adequately reproduced the conditions of the *ex-situ* synthesis and that the NASICON structure can readily form, as the two different synthesis methods produce very similar local structures.

X-ray total scattering overall conclusions

In summary, X-ray total scattering has provided insights into the thermal expansion properties through Rietveld refinements and qualitative analysis of the PDFs, revealing that there is very little expansion in the $Al_xTi_{2-x}(PO_4)_3$ framework in $Li_{1+x}Al_xTi_{2-x}(PO_4)_3$ samples, which prevents expansion along the *a* axis. The structurally robust $Al_xTi_{2-x}(PO_4)_3$ framework remains even in the $Li_3Al_xTi_{2-x}(PO_4)_3$ materials, although the TiO_6 octahedra are slightly different from the $Li_{1+x}Al_xTi_{2-x}(PO_4)_3$ materials due to the increased bond length of Ti^{3+} compared to Ti^{4+}.[35] Rietveld refinements combined with the X-ray PDF data of $Li_3Al_xTi_{2-x}(PO_4)_3$ reveal that there is very little change to the polyhedra locally, showing that the cell expansion comes from the movement of the whole polyhedra, which expand along the *a* axis, causing the *c* axis to shrink analogous to a wine rack. The change in the thermal expansion behavior may be due to the lack of occupancy on the M1 site.[36, 38] Despite adding the additional Li^+ into the NASICON structure, locally there is little change, indicating that the increase in conductivity in $Li_{1+x}Al_xTi_{2-x}(PO_4)_3$ from $x = 0$ to $x = 0.3$ is

due to the increase in the number of Li^+ and that they occupy the M2 site, as previously suggested.[20, 31, 51, 60] The PO_4 locally remain similar even upon insertion of additional Li.

Neutron total scattering

The elements in $Li_{1+x}Al_xTi_{2-x}(PO_4)_3$ and $Li_3Al_xTi_{2-x}(PO_4)_3$ are all weak X-ray scatterers, particularly Li (Z = 3). Additionally, as the X-ray form factor has a dependence on θ, it can be difficult to obtain the correct scaling factor when processing total scattering into PDF data. Therefore, neutron data were collected.

Long-range structure

Bragg scattering neutron data were used to obtain long-range, average structure models. All samples were found to adopt the same symmetry as the starting models described in the Experimental Section above ($Li_{1+x}Al_xTi_{2-x}(PO_4)_3$ = R-3c, $Li_3Al_xTi_{2-x}(PO_4)_3$ = R-3). Initial refinements included Li atoms on the same sites as the starting structural models, described in the Experimental section above, but were later removed. Difference Fourier maps were applied using only bank 2, which has a high d-spacing and therefore sensitivity to the Li atoms. The final Rietveld plots using bank 5 for each sample are given in Figure 6. All structural models obtained give excellent fits to the observed data.

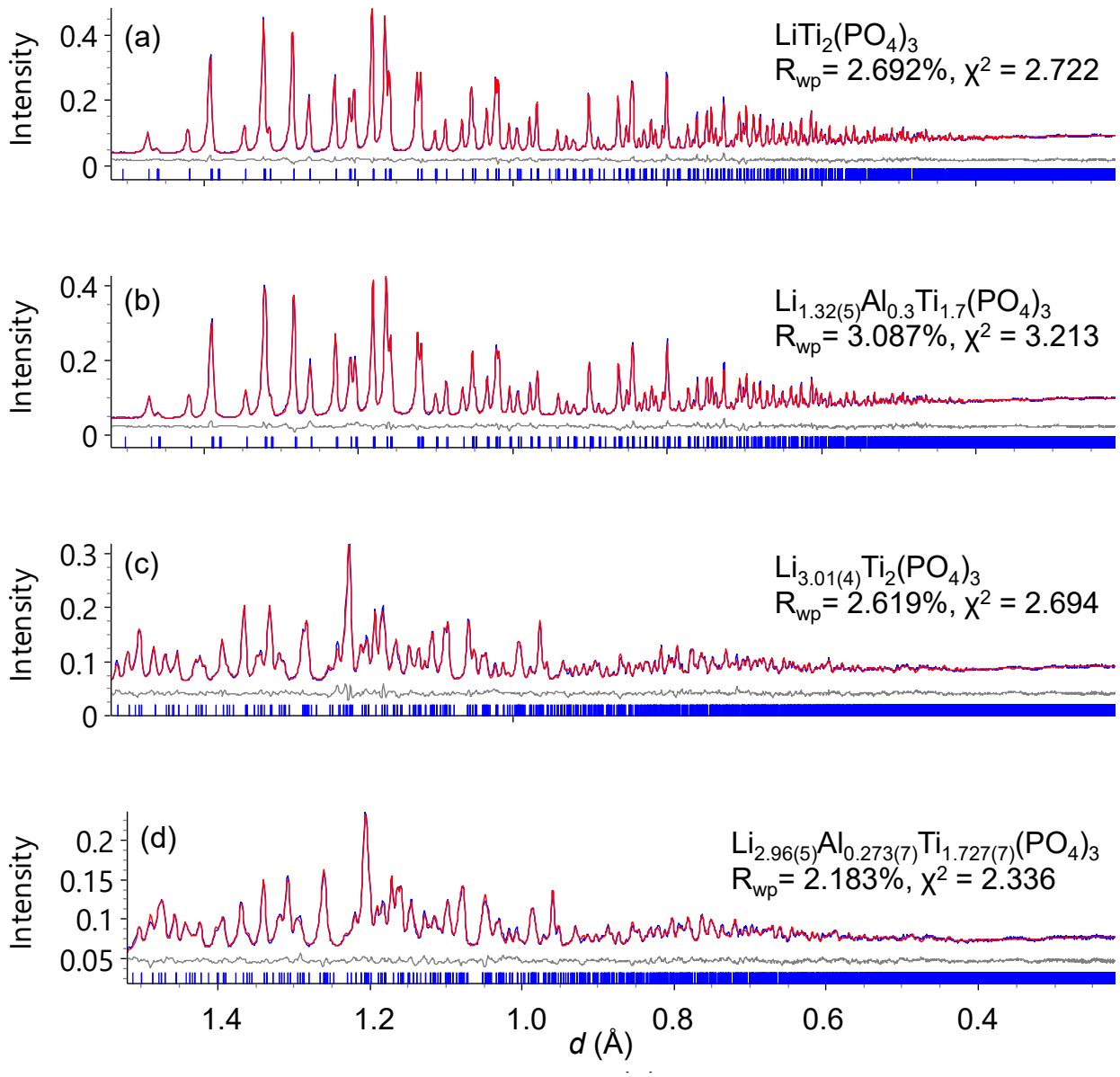

Figure 6 – Neutron Rietveld plots using bank 5 (2θ = 154°). R_{wp} and χ^2 values given in the figure are for the individual bank; (a) $LiTi_2(PO_4)_3$, R_{wp} = 2.847%, χ^2 = 3.125; (b) $Li_{1.32(5)}Al_{0.3}Ti_{1.7}(PO_4)_3$, R_{wp} = 3.334%, χ^2 = 3.762; (c) $Li_{3.01(4)}Ti_2(PO_4)_3$, R_{wp} = 2.207%, χ^2 = 2.578; (d) $Li_{2.96(5)}Al_{0.273(7)}Ti_{1.727(7)}(PO_4)_3$, R_{wp} = 2.181%, χ^2 = 2.339. Blue curves = observed data; red curves = calculated pattern; grey curves = difference between observed data and calculated pattern. Blue tick marks = reflections arising to the NASICON phase.

After applying difference Fourier map to $LiTi_2(PO_4)_3$, one potential location for the Li atoms was on a 12*c* site [(0, 0, *z*)] close to the 6*b* site [(0, 0, 0)], however refining Li on this site with a fractional occupancy of

0.5 resulted in unphysical Li–Ti distances of ~0.76 Å. Therefore, Li was placed with 100% occupancy on the 6*b* site, in agreement with Redhammer *et al*.[51] Crystallographic parameters for $LiTi_2(PO_4)_3$ are presented in Table 1 and selected bond distances are given in Table S1. The isotropic ADP for Li1 is quite large at B = 5.6 Å^2. However, as the Li are quite mobile in this material even at room temperature, this is expected. This may also arise from static disorder caused by Li slowing down during cooling of the sample.

Table 1 – Crystallographic parameters for $LiTi_2(PO_4)_3$. Space group = *R*-3*c*; a = 8.52452(15)Å, c = 20.8687(4) Å, α = 90°, γ = 120°, V = 1313.31(5) Å^3, R_{wp} = 2.847%, χ^2 = 3.125.

Site label	**Wyckoff site**	***x***	***y***	***z***	**Occupancy**	***B* (Å^2)**
Ti1	12*c*	0	0	0.14203(8)	1	0.31(2)
P1	18*e*	0.29106(9)	0	¼	1	0.249(13)
O1	36*f*	0.18517(9)	0.99644(9)	0.19001(2)	1	0.698(13)
O2	36*f*	0.18873(8)	0.16476(7)	0.08096(2)	1	0.509(13)
Li1 (M1)	6*b*	0	0	0	1	5.6(2)

A similar procedure was performed for $Li_{1.3}Al_{0.3}Ti_{1.7}(PO_4)_3$. However, as the Al^{3+} cations occupy the same sites as Ti^{4+}, the occupancies of both atoms were freely refined before searching for the Li^+ location, using fixed Li occupancies and refining coordinates from the model obtained by Pogosova *et al*.[52] During refinement, it was found using separate ADPs for Al and Ti resulted in a divergence, so a single ADP was utilized. This resulted in a Ti occupancy of 0.861(3) and Al occupancy of 0.139(3), similar to the nominal occupancies of 0.85 and 0.15 respectively. As the R_{wp} did not significantly improve (R_{wp} = 3.825% *versus* 3.832), the occupancies were fixed back to 0.85 and 0.15. Both Li ions were removed, and a Fourier difference map was applied, finding the first Li is located on the (0, 0, 0) position. A second difference Fourier map was applied with the Li occupying the M1 site, which found the Li2 on a 36*f* site close to the M2 site [(0.06212, 0.34324, 0.07809)]. A single ADP was used for both Li sites due to divergence of the ADPs into negative values, which also occurred in the refinements of Arbi *et al*.[31] The Li occupancies were set to Li1 = 1.0 and Li2 = 0.05 and allowed to freely refine, resulting in unphysical occupancies of Li1 = 1.33(4), Li2 = 0.176(9) and a total Li of 2.38(7) per formula unit with fitting parameters of R_{wp} = 3.303%,

$\chi^2 = 3.727$. As this resulted in a physically impossible occupancy for Li1, the Li occupancies were reset to Li1 = 1.0 and Li2 = 0.05 and a restraint was added such that the total Li per formula unit should not exceed 1.3, which resulted in Li occupancies of Li1 = 0.85(3), Li2 = 0.077(7) and a total Li of 1.32(5) with fitting parameters of $R_{wp} = 3.334\%$, $\chi^2 = 3.762$. The crystallographic parameters of this structure are given in Table 2 and selected bond distances are given in Table S2. In this model, the Li1 site is partially occupied, which is different from that reported by Pogosova *et al*.,[52] but is in agreement with the models suggested by Redhammer *et al*.,[51] Arbi *et al*.,[60] and Pérez-Estébanez *et al*.[61]

Table 2 – Crystallographic parameters for $Li_{1.32(5)}Al_{0.3}Ti_{1.7}(PO_4)_3$. Space group = *R*-3*c*; $a = 8.5270(2)$ Å, $c = 20.8576(6)$ Å, $\alpha = 90°$, $\gamma = 120°$, $V = 1313.38(8)$ Å^3, $R_{wp} = 3.334\%$, $\chi^2 = 3.762$.

Site label	**Wyckoff site**	***x***	***y***	***z***	**Occupancy**	***B* (Å^2)**
Ti1	12*c*	0	0	0.14202(14)	0.85	0.19(3)
Al1	12*c*	0	0	0.14202(14)	0.15	0.19(3)
P1	18*e*	0.29048(13)	0	¼	1	0.313(18)
O1	36*f*	0.18462(12)	0.99524(12)	0.18975(3)	1	0.863(19)
O2	36*f*	0.18897(11)	0.16453(9)	0.08131(3)	1	0.600(18)
Li1 (M1)	6*b*	0	0	0	0.85(3)	4.5(3)
Li2 (M2)	36*f*	0.063(7)	0.322(10)	0.067(2)	0.077(7)	4.5(3)

For $Li_3Ti_2(PO_4)_3$, the Fourier difference map indicated that the Li atoms were located on the M2 and M3' sites, with no Li being found in the M1 sites. Much like with $Li_{1.3}Al_{0.3}Ti_{1.7}(PO_4)_3$, freely refining the Li occupancies from 0.5 each resulted in a Li-ion excess of 3.7(4) per formula unit. Applying a restraint such that the total content of Li per formula unit is 3 and starting from occupancies of 0.5 each resulted in a total Li content of 3.01(4) and a very slight improvement of the fit ($R_{wp} = 2.207\%$ *versus* 2.221%, $\chi^2 = 2.578$ *versus* 2.594). When the Li atomic coordinates were refined, the structure is very similar to that reported by Aatiq *et al*.[33] The crystallographic parameters are in Table 3 and selected bond distances are given in Table S3.

Table 3 – Crystallographic parameters for $Li_{3.01(4)}Ti_2(PO_4)_3$. Space group = *R*-3; $a = 8.4013(3)$ Å, $c = 22.9122(9)$ Å, $\alpha = 90°$, $\gamma = 120°$, $V = 1400.53(12)$ Å^3, $R_{wp} = 2.207\%$, $\chi^2 = 2.578$.

Site label	Wyckoff site	*x*	*y*	*z*	Occupancy	*B* (Å^2)
Ti1	6*c*	0	0	0.14365(18)	1	0.55(6)
Ti2	6*c*	0	0	0.34734(18)	1	0.12(5)
P1	18*f*	0.29082(16)	–0.00124(19)	0.25119(7)	1	0.007(13)
O1	18*f*	0.16633(16)	0.21668(18)	0.09011(5)	1	0.34(2)
O2	18*f*	0.13716(17)	0.2306(2)	0.39855(3)	1	0.63(3)
O3	18*f*	0.19566(19)	0.99329(17)	0.19356(6)	1	1.18(3)
O4	18*f*	0.91010(15)	0.14580(17)	0.29960(5)	1	0.81(3)
Li1 (M3)	18*f*	0.3597(6)	-0.0198(6)	0.71091(19)	0.809(11)	0.37(6)
Li2 (M3')	18*f*	0.277(3)	0.030(3)	0.4533(9)	0.195(10)	0.37(6)

In this study, the Li1 atom was found to be located on (0.3597(6), –0.0198(6), 0.71091(19)) and Li2 atom on (0.277(3), 0.030(3), 0.4533(9)), compared to Li1 on (0.030(4), 0.319(4) 0.045(1)) and Li2 on (0.055(8), 0.373(9), 0.117(3))). The coordinates are also in excellent agreement with the structure reported by Zhang *et al*. [Li1 = (0.02350, 0.30090, 0.04360), Li2 = (0.09500, 0.41700, 0.08680),[30] as well as Arbi *et al*.[31] This indicates that these sites are highly favorable locations for the Li^+ cations in the fully lithiated sample. There are differences in the occupancies of the Li1 and Li2 sites in this study compared to those obtained by Aatiq *et al*.[33] and Zhang *et al*.[30] where the Li2 in this study is less populated (Li2 = 0.195(10)), *c.f*. 0.34(6)[33] and 0.313[30]). Additionally, the ADP of P is quite low (*B* = 0.007(13) Å^2) and initially refined to a negative value. This occurred during the refinements of Arbi *et al*.[31]

In the analysis of $Li_3Al_{0.3}Ti_{1.7}(PO_4)_3$, initially the Li sites and occupancies as found by Arbi *et al*.[31] were maintained and the Al and Ti occupancies were refined. In the *R*-3 space group, there are two Ti/Al sites. Refining with separate ADPs for both sites resulted in some negative thermal parameters, so a constraint was applied where a single ADP was utilized for the Ti and Al sites. Freely refining the occupancies of Ti and Al resulted in a total Ti and Al per formula unit of 1.763(7) and 0.237(7) with a fit of R_{wp} = 2.192% and χ^2 = 2.351. Applying a constraint of $Al_{occ} = 1 - Ti_{occ}$ resulted in a total content of Ti = 1.727(7), Al = 0.273(7) per formula unit, with a fit of R_{wp} = 2.199%, χ^2 = 2.358. As the fits are very close, the latter composition ($Ti_{1.727(7)}Al_{0.273(7)}$) was selected. A similar difference in the nominal and refined occupancies was seen with the un-lithiated sample of $Li_{1.32(5)}Al_{0.3}Ti_{1.7}(PO_4)_3$, from which this sample is derived.

Therefore, it is possible that amorphous $AlPO_4$ is present, explaining the minor deficiency in Al seen in the refinement. After removing the Li sites and using Fourier difference maps to place them back, Li atoms were once again found to occupy the M3 and M3' sites. The occupancies were freely refined and converged to a total Li content of 2.96(5) per formula unit. This is within 1σ of the nominal composition of Li. Therefore, no restraints were applied to the occupancies. The ADP for the P site initially refined to a negative value (–0.001(15) Å^2). Therefore, in a subsequent refinement the cell parameters, atomic coordinates and ADPs of all sites were fixed. The P ADP was set to a small, positive value of 0.005 Å^2 and allowed to freely refine, resulting in a value of 0.004(13) Å^2. This is still a small value with a large error, but is similar to the value obtained for $Li_{3.01(4)}Ti_2(PO_4)_3$ (Table 3). The crystallographic parameters are given in Table 4 and selected bond distances are given in Table S4.

Table 4 – Crystallographic parameters for $Li_{2.96(5)}Al_{0.273(7)}Ti_{1.727(7)}(PO_4)_3$. Space group = *R*-3; a = 8.3570(5) Å, c = 22.7300(13) Å, α = 90°, γ = 120°, V = 1374.79(18) Å^3, R_{wp} = 2.181%, χ^2 = 2.339.

Site label	**Wyckoff site**	***x***	***y***	***z***	**Occupancy**	***B* (Å^2)**
Ti1	6*c*	0	0	0.1416(3)	0.870(5)	0.17(5)
Al1	6*c*	0	0	0.1416(3)	0.130(5)	0.17(5)
Ti2	6*c*	0	0	0.3468(3)	0.856(5)	0.17(5)
Al2	6*c*	0	0	0.3468(3)	0.144(5)	0.17(5)
P1	18*f*	0.29117(18)	-0.0007(2)	0.25170(8)	1	0.004(13)
O1	18*f*	0.16523(19)	0.2146(2)	0.09008(6)	1	0.35(3)
O2	18*f*	0.1368(2)	0.2311(2)	0.39921(6)	1	0.54(3)
O3	18*f*	0.1924(2)	0.9941(2)	0.19335(7)	1	1.20(4)
O4	18*f*	0.90925(17)	0.1448(2)	0.30040(6)	1	0.69(3)
Li1 (M3)	18*f*	1.0215(7)	0.3822(7)	0.7127(2)	0.807(13)	0.31(9)
Li2 (M3')	18*f*	0.022(3)	0.351(3)	0.1198(12)	0.179(11)	0.31(9)

Local structure

The long-range structures provided a starting point for PDF refinements. Small box modelling was performed in order to elucidate the local structure of $Li_{1+x}Al_xTi_{2-x}(PO_4)_3$ and $Li_3Al_xTi_{2-x}(PO_4)_3$ (x = 0, 0.3). Figure 7 gives the final small box fits for these materials. The structural parameters are given in the SI.

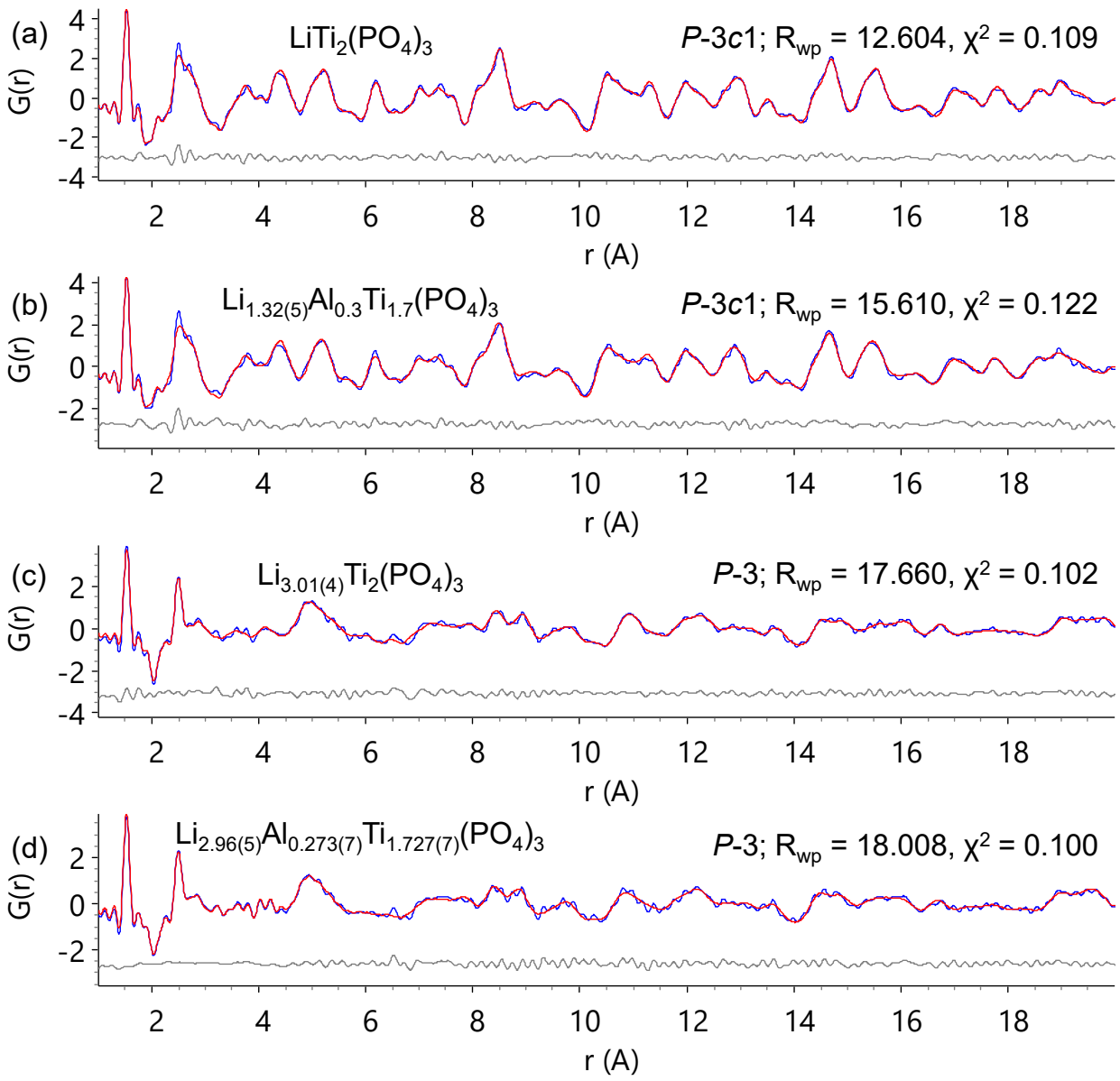

Figure 7 – Small box neutron PDF refinements for: (a) $LiTi_2(PO_4)_3$; (b) $Li_{1.32(5)}Al_{0.3}Ti_{1.7}(PO_4)_3$; (c) $Li_{3.01(4)}Ti_2(PO_4)_3$; (d) $Li_{2.96(5)}Al_{0.273(7)}Ti_{1.727(7)}(PO_4)_3$. Blue curve = observed PDF, red curve = calculated PDF, grey curve = difference between observed and calculated PDFs. The space group used in the refinement is given in each figure.

For $LiTi_2(PO_4)_3$, the parent *R*-3*c* space group was initially used. As the function used to model the effect of ADPs on the PDF is more strongly weighted at low *r*, the first refinements were performed using r_{max} = 10 Å. The *r*-dependent component of the function was then fixed, and the maximum range was expanded to r_{max} = 20 Å, resulting in a fit of R_{wp} = 15.211% and χ^2 = 0.129 (Figure S8a). The procedure was repeated

using a cell with the space group of *R*-3, which was generated from the starting model using ISODISTORT.[56] Materials have previously been found to have a locally lower symmetry than the apparent long-range structure, such as $Ba_2In_{1.7}P_{0.2}O_{5.2}$,[62] and Fe_3N.[57] This represents a local loss of the *c* glide plane and is the space group adopted by the lithiated samples. It provides some more degrees of freedom by adding additional crystallographically independent atomic sites. The refinement using *R*-3 resulted in a marginal improvement in the fit (Figure S8b) with R_{wp} = 14.300%, χ^2 = 0.123. Finally, a third refinement was also performed using a *P*-3*c*1 starting model. By removing the rhombohedral centering, there are now more independent atomic sites, some of which also have more degrees of freedom with regards to certain coordinates, *e.g.* the Li1, which sits on a 6*b* (0, 0, 0) site in the *R*-3*c* space group is split into two sites on a 2*b* (0, 0, 0) site and a 4*d* (1/3, 2/3, *z*) site in the *P*-3*c*1 space group and the Ti atom on a single 12*c* site in *R*-3*c* is split onto 3 sites: one 4*c* site (0, 0, *z*) and two 4*d* sites. A better fit was obtained of R_{wp} = 12.604%, χ^2 = 0.109 (Figure 7a). There is a minor discrepancy between the calculated PDF and the observed PDF at *r* = 2.5 and 2.7 Å, corresponding to the O–O nearest neighbors. This discrepancy arises due to the very strong correlations of the P–O nearest neighbors, as it can be fit when that peak is excluded. This minor discrepancy could potentially be removed with a more complicated thermal parameter function than the one employed in this study, however the fit is sufficient. Table S5 gives the structural parameters obtained from this refinement. The first peak at *r* ≈1.53 corresponds to the P–O distances in PO_4 tetrahedra, which is in good agreement with the average bond distance found in the Rietveld refinements (Table S1). The next is a broad, weak peak starting at *r* ≈ 1.75 Å extending to ~2.0 Å. The range of 1.85 < *r* < 2.01 Å corresponds to the Ti–O in the TiO_6 octahedra, which are weak due to the negative scattering length of Ti (*b* = –3.438 fm) and positive scattering factor of O (*b* = 5.803 fm).

A similar process was applied to $Li_{1.3}Al_{0.3}Ti_{1.7}(PO_4)_3$, where the best obtained fit was using *P*-3*c*1 again (see Figure S9 for a comparison between *R*-3*c*, *R*-3 and *P*-3*c*1). In this refinement (Figure 7b), the Al and Ti occupancies remained fixed. As there are 3 Ti/Al sites in the *P*-3*c*1 structure, a refinement was performed where the occupancies of Al and Ti were refined to determine if there is any local clustering. The three sites

all approximately had occupancies of 0.85 for Ti and 0.15 for Al, which match the occupancies expected for an even distribution. Therefore, at this level of Al-doping, there is no apparent clustering of Al and Ti. The refinement with fixed Ti and Al occupancies is given in Figure 7b and the structural parameters are given in Table S6. The local structures of $Li_{1+x}Al_xTi_{2-x}(PO_4)_3$ (x = 0, 0.3) are remarkably similar to each other, with the first peak corresponding to the PO_4 tetrahedra also being located at $r \approx 1.53$ Å and the Ti/Al–O peak at $1.75 \leq r \leq 2.0$ Å, indicating that the 0.3 Al has not significantly altered the Ti/AlO_6 octahedra. It also shows the strength of the bonds of the PO_4 tetrahedra, as altering the TiO_6 octahedra and the additional 0.3 Li per formula have not affected their bond distances. This explains the origin of the increased conductivity in the x = 0.3 material compared to the x = 0 material;[12, 32, 63] the increased number of Li^+ cations does not affect the local NASICON structure, instead providing additional charge carriers as well as adding Li^+ ions to the high-multiplicity (36*f*), fast conducting M2 site.

The local structure of $Li_3Ti_2(PO_4)_3$ (Figure 7c) is more ordered than that of $LiTi_2(PO_4)_3$, particularly the O^{2-} sublattice ($2.5 \leq r \leq 3.0$ Å). Therefore, a more complicated function was employed to model the effects of ADPs, which uses different values for atoms within a sphere of a given radius, where that radius is also refined. Furthermore, there was a more significant difference in the fit when changing from *R*-3 symmetry to *R*3 and *P*-3 symmetry (Figure S10), where the fit improved from R_{wp} = 23.606%, χ^2 = 0.135 with *R*-3 to R_{wp} = 18.170, χ^2 = 0.104 for *R*3 and R_{wp} = 17.660%, χ^2 = 0.102 for *P*-3. Specifically, the Li–O and O–O nearest neighbor distances were fit better with the lower symmetry. As the *P*-3 space group results in an overall better fit at r = 2.25 Å and r = 4.10 Å, the *P*-3 space group was selected. Lowering the symmetry from *R*-3 to *P*-3 results in tripling the number of symmetrically independent atomic sites. Due to the large number of atomic sites, some anti-bumping restraints of 1.9 Å were applied to two Li–O pairs (Li2_3–O2_3 and Li2_1–O2_1) in order to prevent unphysical distances from being generated by the refinement. Although this model resulted in a Li–O distance of 1.89(8) Å and a Li–O of 1.8(4) Å, as well as a single short Ti–O distance of 1.81(3) Å, the other distances are physically sensible, with no short cation-cation distances, indicating that the fit is physically reasonable. The structural parameters are given in Table S7.

The first peak corresponding to the PO_4 tetrahedra is once again at $r \approx 1.53$ Å. This shows another way in which the PO_4 units are strong, as not only do the P–O bond lengths experience little change with thermal expansion as seen with the *in-situ* XPDF data, but they also do not expand much when the lithium content is greatly increased from 1 Li atom per formula unit to 3 Li atoms per formula unit. In comparison to $LiTi_2(PO_4)_3$, there is a noticeable peak at $r \approx 1.90$ Å, indicating increased order within the Ti–O distances in the TiO_6 octahedra. The bond distances have also increased to approximately 2.0 Å due to the reduction of Ti^{4+} to Ti^{3+}, increasing the bond length.[35] These results reveal why $Li_3Ti_2(PO_4)_3$ has been reported to have a higher ionic conductivity[30] than $LiTi_2(PO_4)_3$: despite there being a more complicated oxide sublattice, the $Ti_2(PO_4)_3$ framework locally experiences very little change, meaning that the Li^+ charge carriers experience very little hinderance. Additionally, there are three times the number of Li^+ cations and they occupy the M3 and M3' sites, which can be hopped to easily in comparison from the M1 site.

The same procedure was performed for $Li_3Al_{0.3}Ti_{1.7}(PO_4)_3$, where using the *P*-3 symmetry (Figure 7d) resulted in the best fit of $R_{wp} = 18.008\%$, $\chi^2 = 0.100$ (see Figure S11 for a comparison between *R*-3, *R*3 and *P*-3). Intriguingly, the fit using *R*3 was notably worse ($R_{wp} = 22.075\%$, $\chi^2 = 0.122$) than the fit with *P*-3, particularly regarding the range $4 \leq r \leq 6$ Å, which corresponds to the second-nearest neighbor distances and O–O sublattice. This indicates that the substitution of Al onto the Ti site may have induced some additional order local, possibly due to the greater difference in ionic radii of Ti^{3+} (0.670 Å) with Al^{3+} (0.535 Å) compared to Ti^{4+} (0.605 Å).[35] As the Al sites appeared to be evenly distributed in $Li_{1.3}Al_{0.3}Ti_{1.7}(PO_4)_3$, the Al and Ti site occupancies were not refined due to the complexity of the *P*-3 structure. Once again, anti-bumping restraints of 1.9 Å were applied to two Li–O pairs (Li2_1–O3_3 and Li2_3–O3_3). This resulted in one Li–O distance of 1.78(4) Å and one of 1.83(4) Å. There are no other short distances in this model. The structural parameters are given in Table S8. This structure is very similar to $Li_3Ti_2(PO_4)_3$, indicating that the doping of 0.3 Al per formula unit on the Ti sites has not greatly affected the structure.

The structural parameters obtained from these refinements can be used to quantify the degree of distortion of the polyhedra. One such parameter is τ_4', defined by Okuniewski *et al.*[64] as:

$$\tau_4' = \frac{\beta - \alpha}{360 - \theta} + \frac{180 - \beta}{180 - \theta} \qquad \text{(Equation 1)}$$

Where α and β are the two largest angles ($\beta > \alpha$) and $\theta = \cos^{-1}(1/3) \approx 109.5°$, *i.e.* the ideal tetrahedral bond angle. This means that τ_4' = 0 corresponds to a perfect square planar geometry and τ_4' = 1 corresponds to a perfect tetrahedral geometry. Table 5 shows the τ_4' parameters obtained from the neutron Rietveld and PDF small box refinements.

Table 5 – τ_4' parameters obtained for $Li_{1+x}Al_xTi_{2-x}(PO_4)_3$ and $Li_3Al_xTi_{2-x}(PO_4)_3$ (x = 0, 0.3) from neutron Rietveld and PDF small box refinements

	$LiTi_2(PO_4)_3$	**$Li_{1.3}Al_{0.3}Ti_{1.7}(PO_4)_3$**	**$Li_3Ti_2(PO_4)_3$**	**$Li_3Al_{0.3}Ti_{1.7}(PO_4)_3$**
P1 (Rietveld)	0.985(4)	0.987(5)	0.980(14)	0.972(17)
P1_1 (PDF)	0.91(6)	0.94(15)	1.0(3)	0.9(2)
P1_2 (PDF)	0.96(5)	0.95(11)	0.9(3)	0.9(2)
P1_3 (PDF)	N/A	N/A	0.9(3)	0.9(2)
P_{mean} (PDF)	0.94(4)	0.95(5)	0.93(17)	0.94(12)

There is very little change in the τ_4' parameters across the series, even locally, where the PO_4 in all materials exhibit essentially ideal tetrahedral geometry. This indicates a degree of rigidity of the PO_4 tetrahedra, as it has been previously reported that there are distortions within the PO_4 tetrahedra as temperature increases.[36] While these data were all collected at room temperature, they still reveal that the increase in Li^+ content is not sufficient enough to heavily, locally distort the PO_4 tetrahedra. These factors are likely key to the unusual thermal expansion behavior as well as enabling the fast conductivity as the Li^+ content is increased, even to very large degrees.

Conductivity

EIS was performed on pressed pellets of $Li_{1+x}Al_xTi_{2-x}(PO_4)_3$ and $Li_3Al_xTi_{2-x}(PO_4)_3$ (x = 0, 0.3) in order to determine if $Li_{1.3}Al_{0.3}Ti_2(PO_4)_3$ would have a higher conductivity than $LiTi_2(PO_4)_3$[11-16] and if $Li_3Ti_2(PO_4)_3$

would have a higher conductivity than $LiTi_2(PO_4)_3$ as previously reported,[30] in order to correlate the structure with the conductivity. As Li loss in LATP is known to occur above 950 °C,[65] and $Li_3Al_xTi_{2-x}(PO_4)_3$ samples were shown to decompose in air at 500 °C (see Figure 3), powder patterns were obtained on separate pellets sintered at 1200 °C for $Li_{1+x}Al_xTi_{2-x}(PO_4)_3$ and on the pellets of $Li_3Al_xTi_{2-x}(PO_4)_3$ sintered at 800 °C after EIS measurements (Figure S12). As can be seen from Figure S12a and Figure S12b, $Li_{1+x}Al_xTi_{2-x}(PO_4)_3$ is still the dominant phase, although Li-loss did occur, which is evident from the visible TiO_2 impurity (2.76(5)% for $x = 0$ and 1.83(7)% for $x = 0.3$). Such high sintering temperatures were necessary as a robust pellet for the $x = 0$ sample could not be obtained at 950 °C. Table 6 gives the ionic conductivity of these samples, while Figure 8 shows the Nyquist plots.

Table 6 – Conductivities of $Li_{1+x}Al_xTi_{2-x}(PO_4)_3$ and $Li_3Al_xTi_{2-x}(PO_4)_3$ ($x = 0$, 0.3) obtained at 23 °C.

Sample	**Sintering temp (°C)**	σ_{lat} **(S cm^{-1})**	σ_{gb} **(S cm^{-1})**	σ_{elec} **(S cm^{-1}**	σ_{total} **(S cm^{-1})**
$LiTi_2(PO_4)_3$	1200	Undetermined	1.492×10^{-5}	Undetermined	1.569×10^{-5}
$Li_{1.3}Al_{0.3}Ti_{1.7}(PO_4)_3$	1200	8.574×10^{-4}	2.544×10^{-4}	Undetermined	1.962×10^{-4}
$Li_{1.3}Al_{0.3}Ti_{1.7}(PO_4)_3$	950	Undetermined	6.100×10^{-6}	Undetermined	6.100×10^{-6}
$Li_3Ti_2(PO_4)_3$	925	Undetermined	2.390×10^{-7}	1.232×10^{-7}	8.130×10^{-8}
$Li_3Ti_2(PO_4)_3$	800	Undetermined	Undetermined	1.830×10^{-8}	1.830×10^{-8}
$Li_3Al_{0.3}Ti_{1.7}(PO_4)_3$	800	Undetermined	1.106×10^{-7}	5.693×10^{-8}	3.759×10^{-8}

$LiTi_2(PO_4)_3$ was found to possess a total conductivity of 1.492×10^{-5} S cm^{-1}, which is higher than that reported by Aono *et al.*[13] (2×10^{-6} S cm^{-1}) and Pinus *et al.*[20] (5.8×10^{-7} S cm^{-1}), and similar to that reported by Zhang *et al.*[30] (1.01×10^{-5} S cm^{-1}) $Li_{1.3}Al_{0.3}Ti_{1.7}(PO_4)_3$ achieved a good lattice conductivity $\sigma_{lat} = 8.574 \times 10^{-4}$ S cm^{-1}, which is about 3.5 times lower than that reported by Aono *et al.*[13] (3×10^{-3} S cm^{-1}) and 6 times lower than that reported by Rettenwander *et al.*[15] (5.14×10^{-3} S cm^{-1}) and Arbi *et al.*[32] (5.1×10^{-3} S cm^{-1} for $x = 0.2$), but the grain boundary ($\sigma_{gb} = 2.544 \times 10^{-4}$ S cm^{-1}) and total ($\sigma_{tot} = 1.962 \times 10^{-4}$ S cm^{-1}) are very similar ($\sigma_{gb} = 9 \times 10^{-4}$, $\sigma_{tot} = 7 \times 10^{-4}$ S cm^{-1} reported by Aono *et al.*[13] and σ_{gb} $\sigma_{tot} = 5.2 \times 10^{-5}$ S cm^{-1} from Arbi *et al.*[32]). This confirms that doping with Al^{3+} has indeed improved the conductivity. It should be noted that the $Li_{1.3}Al_{0.3}Ti_{1.7}(PO_4)_3$ pellet that was sintered at only 950 °C could only be fit with one resistive element, which we assign as a grain boundary response (see Figure S13a for the Nyquist plot),

resulting in a total conductivity of 6.100×10^{-6} S cm^{-1}. This demonstrates the importance of sintering temperature in producing highly-conducting pellets. As $Li_3Al_xTi_{2-x}(PO_4)_3$ is prone to oxidation at temperatures above 450 °C (see Figure 3), the pellets were sintered under flowing Ar. Heating at 925 °C resulted in a noticeable color change (Figure S1b) to a deeper lavender/grey for both samples, while the $x = 0.3$ sample melted and showed signs of gas emission. EIS performed on the $Li_3Ti_2(PO_4)_3$ pellet at 925 °C showed that it is a poor ionic conductor with $\sigma_{gb} = 2.390 \times 10^{-7}$ S cm^{-1} and an electronic component, assigned as there is no sign of a blocking electrode feature, of $\sigma_{elec} = 1.327 \times 10^{-7}$ S cm^{-1}. However, the sample decomposed (discussed below), so this conductivity is not representative of the inherent conductivity of $Li_3Ti_2(PO_4)_3$. Pellets were obtained at 800 °C and EIS was performed on these samples, however XRD revealed a complete decomposition of $Li_3Al_xTi_{2-x}(PO_4)_3$ (Figure S12c and Figure S12d). Both of the resulting compositions are likely electronic conductors as no blocking electrode feature can be determined from the impedance spectra. For $x = 0$, there is only one response, resulting in a conductivity of $\sigma_{elec} = \sigma_{tot} = 1.830 \times 10^{-8}$ S cm^{-1}. For $x = 0.3$, two elements can be fit, which we assign to grain boundary conductivity ($\sigma_{gb} = 1.106 \times 10^{-7}$ S cm^{-1}) and electronic conductivity ($\sigma_{elec} = 5.693 \times 10^{-8}$), giving a total conductivity of $\sigma_{tot} = 3.759 \times 10^{-8}$ S cm^{-1}.

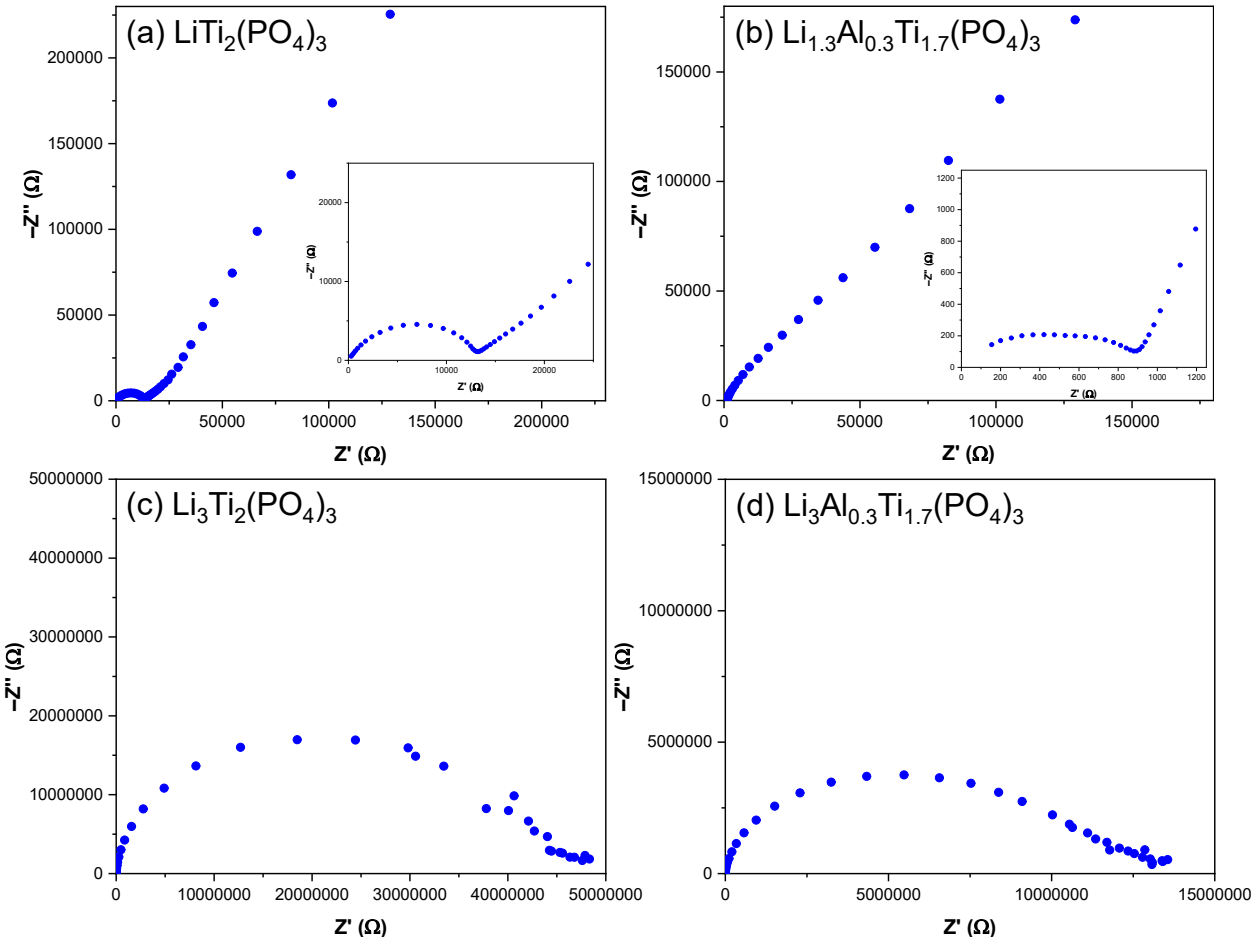

Figure 8 – Nyquist plots for (a) $LiTi_2(PO_4)_3$ and (b) $Li_{1.3}Al_{0.3}(PO_4)_3$ heated at 1200 °C for 2 h; insets of the low *Z*' regions are included; (c) $Li_3Ti_2(PO_4)_3$ and (d) $Li_3Al_{0.3}Ti_{1.7}(PO_4)_3$ heated at 800 °C for 2 h under Ar.

As $Li_3Al_xTi_{2-x}(PO_4)_3$ decomposed when sintering, we used a PEEK pressure cell to cold press and maintain constant pressure. Both patterns (Figure S13c and Figure S13d) show straight lines indicative of a pure dielectric capacitor. This behavior was likely observed because the powders, which consist of very fine grains, did not cold press very well, hindering Li-ion mobility.

Zhang *et al.*[30] reported that $Li_3Ti_2(PO_4)_3$ has an ionic conductivity 1 order of magnitude higher than $LiTi_2(PO_4)_3$ (1.9×10^{-4} S cm^{-1} and 1.01×10^{-5} S cm^{-1}, respectively), which they attribute to the additional Li^+ charge carriers. On the other hand, Arbi *et al.*[31] suggested through solid-state NMR that the additional Li^+ cations in $Li_3Al_{0.3}Ti_{1.7}(PO_4)_3$ hinder Li-ion mobility in comparison to $Li_{1.3}Al_{0.3}Ti_{1.7}(PO_4)_3$, although there

is definite Li-ion mobility at 350 K. They also state that the Al-doped sample has a slightly higher Li-ion mobility than $Li_3Ti_2(PO_4)_3$. Although we could not directly measure the conductivities of the fully-lithiated samples, the conductivities we obtained for $Li_{1.3}Al_{0.3}(PO_4)_3$ (σ_{lat} = 8.574 × 10^{-4} S cm^{-1} and σ_{tot} = 1.962 × 10^{-4} S cm^{-1}) are higher than that reported by Zhang *et al*.[30] for $Li_3Ti_2(PO_4)_3$, and others have reported $Li_{1.3}Al_{0.3}Ti_{1.7}(PO_4)_3$ with a lattice conductivity of 3 × 10^{-3} S cm^{-1}.[13] It is therefore possible that the increased content of Li^+ ions in $Li_3Ti_2(PO_4)_3$ improves the Li-ion mobility compared to $LiTi_2(PO_4)_3$, as the energy barrier for Li^+ cations to jump from M1 to M1' to M1 sites is larger than that for M3 to M3' to M3 sites,[30] but there is some hinderance of Li-ion mobility due to the large number of Li ions. Our total scattering results suggest that the ability of the $Ti_2(PO_4)_3$ framework to accommodate additional Li^+ cations in the M2 and M3 sites results in these sites maintaining their energy barriers. The migration pathway in $Li_3V_2(PO_4)_3$ (space group: *R*-3) is also similar to $Li_3Ti_2(PO_4)_3$,[66] which suggests that the "structural robustness" of the PO_4 tetrahedra is key to enabling fast Li^+ diffusion by maintaining similar local structure despite changes in Li^+ content and transition metal identities.

Conclusions

VT and *in-situ* X-ray and ambient neutron total scattering experiments have been performed on $Li_{1+x}Al_xTi_{2-x}(PO_4)_3$ and $Li_3Al_xTi_{2-x}(PO_4)_3$ (x = 0, 0.3), elucidating the local structure. The results reveal that the polyhedra in the $Al_xTi_{2-x}(PO_4)_3$ framework experience very little thermal expansion of the nearest-neighbor bonds. Additionally, these polyhedra also do not expand as the number Li^+ cations increases, with the PO_4 tetrahedra additionally showing very little distortion, revealed by maintaining ideal tetrahedral τ_4' values. The VT X-ray total scattering reveals that the near-zero thermal expansion along the *a* axis in $Li_{1+x}Al_xTi_{2-x}(PO_4)_3$ is not only a long-range phenomenon, but also occurs locally with the PO_4 and TiO_6 polyhedra, revealing that the Li^+ most likely move along the *c* axis as it expands. For $Li_3Al_xTi_{2-x}(PO_4)_3$, VT X-ray total scattering shows that there is also little change locally with the polyhedra as the temperature increases, despite there being polynomial PTE along *a* and NTE along *c*, indicating that the whole unit of polyhedra are moving closer along *c* as they move away from each other along *a*. Ambient neutron total scattering

produced refined models of the local structure, further confirming that the increase in Li^+ cations has little effect on the $Ti_2(PO_4)_3$ framework, despite producing a more complicated local oxide sublattice in $Li_3Al_xTi_{2-x}(PO_4)_3$, suggesting that the increase in conductivity despite the symmetry lowering is due to the structural robustness of the NASICON framework permitting an increase in charge carriers without hindering their transport through the structure. These results show how promising phosphate-based framework materials can be for producing new Li-ion conductors, which can be used for further materials discovery and may even extend into other ionic conductors, such as Na-ion conductors. This near-zero thermal expansion along the *a* cell also has implications for solid-state battery manufacturing and processing: if LATP is implemented into the cell using heating, it will expand along the *c* axis, but not along *a*, which could potentially cause cracking if the other components do not match. A material that shows negative thermal expansion along *c* could be implemented with the LATP to produce-near zero thermal expansion, or single crystals cut to produce (*h* 0 0) surfaces could also result in near-zero thermal expansion, both during processing and operating at elevated temperatures. Finally, *in-situ* X-ray total scattering of the sol-gel synthesis reveals that the NASICON framework can locally form at low (300 °C) temperatures and that it crystallizes at higher temperatures, which shows that the NASICON structure is highly favorable to form. This is further confirmed by the neutron Rietveld refinements, which showed excellent agreement with the literature structures previously reported across the $Li_{1+x}Al_xTi_{2-x}(PO_4)_3$ and $Li_3Al_xTi_{2-x}(PO_4)_3$ (x = 0, 0.3) series.

Author contributions

M. S. Chambers and G. M. Veith designed and led the project and wrote and revised the manuscript. G. M. Veith acquired the funding for the project. M. S. Chambers synthesized the materials, collected X-ray and EIS data and performed Rietveld and small box analysis. J. Liu collected neutron data and assisted with analysis of neutron data. O. J. Borkiewicz collected X-ray total scattering data and assisted with data processing. K. J. Llopart and R. L. Sacci collected and assisted with the analysis of EIS data.

Conflicts of Interest

There are no conflicts of interest to report.

Data availability statement

TOPAS input files for the small box PDF refinements of $Li_3Ti_2(PO_4)_3$ and $Li_3Al_{0.3}Ti_{1.7}(PO_4)_3$ have been included as part of the supplementary data.

Crystallographic data for $LiTi_2(PO_4)_3$, $Li_{1.3}Al_{0.3}Ti_{1.7}(PO_4)_3$, $Li_3Ti_2(PO_4)_3$ and $Li_3Al_{0.3}Ti_{1.7}(PO_4)_3$ have been deposited at the ICSD under Deposition Numbers 2363482, 2363483, 2363484 and 2363485 respectively.

Acknowledgements

The authors thank Katie Browning for providing advice with producing large pellets for the solid-state synthesis of $Li_{1+x}Al_xTi_{2-x}(PO_4)_3$ (x = 0, 0.3). The authors also thank Rebecca McAuliffe for assisting with sample preparation at 11-ID-B and for providing feedback on an early draft of this manuscript. This work was also supported as part of GENESIS: A Next Generation Synthesis Center, an Energy Frontier Research Center funded by the U.S. Department of Energy, Office of Science, Basic Energy Sciences under Award Number DESC0019212. This manuscript has been authored by UT-Battelle, LLC under Contract no. DE-AC05-00OR22725 with the U.S. Department of Energy. The United States Government retains and the publisher, by accepting the article for publication, acknowledges that the United States Government retains a nonexclusive, paid-up, irrevocable, world-wide license to publish or reproduce the published form of this manuscript, or allow others to do so, for United States Government purposes. The Department of Energy will provide public access to these results of federally sponsored research in accordance with the DOE Public Access Plan (http://energy.gov/downloads/doepublic-access-plan). This research used resources of the Advanced Photon Source, a U.S. Department of Energy (DOE) Office of Science user facility operated for the DOE Office of Science by Argonne National Laboratory under Contract No. DE-AC02-06CH11357. This used resources at the Spallation Neutron Source, a DOE Office of Science User Facility operated by the Oak Ridge National Laboratory. The beam time was allocated to NOMAD on proposal number IPTS-30563.1.

References

1. K. J. Kim, M. Balaish, M. Wadaguchi, L. Kong and J. L. M. Rupp, Solid-State Li–Metal Batteries: Challenges and Horizons of Oxide and Sulfide Solid Electrolytes and Their Interfaces, *Advanced Energy Materials*, 2021, **11**, 2002689.
2. Y. Tian, G. Zeng, A. Rutt, T. Shi, H. Kim, J. Wang, J. Koettgen, Y. Sun, B. Ouyang, T. Chen, Z. Lun, Z. Rong, K. Persson and G. Ceder, Promises and Challenges of Next-Generation "Beyond Li-ion" Batteries for Electric Vehicles and Grid Decarbonization, *Chemical Reviews*, 2021, **121**, 1623-1669.
3. J. Janek and W. G. Zeier, Challenges in speeding up solid-state battery development, *Nature Energy*, 2023, **8**, 230-240.
4. X. Feng, H. Fang, N. Wu, P. Liu, P. Jena, J. Nanda and D. Mitlin, Review of modification strategies in emerging inorganic solid-state electrolytes for lithium, sodium, and potassium batteries, *Joule*, 2022, **6**, 543-587.
5. Z. Lu, Z. Chen, M. Wang, Y. Wan, J. Yan, S. Chen, Y. Shen, Z. Yan and D. Wang, Roles of Lithium Aluminum Titanium Phosphate in Lithium Batteries, *ACS Applied Energy Materials*, 2023, DOI: 10.1021/acsaem.2c04006.
6. A. Lakshmanan, R. Gurusamy and S. Venkatachalam, Enhanced total ionic conductivity of NASICON-type solid-state electrolyte $Li_{1+x}Al_xTi_{2-x}(PO_4)_3$, *Ionics*, 2023, **29**, 5123-5138.
7. C. Miao, Z. Kou, J. Li, C. Liu, Q. Chen, Y. Xiang and W. Xiao, LiF-doped $Li_{1.3}Al_{0.3}Ti_{1.7}(PO_4)_3$ superionic conductors with enhanced ionic conductivity for all-solid-state lithium-ion batteries, *Ionics*, 2022, **28**, 73-83.
8. A. Mashekova, Y. Baltash, M. Yegamkulov, I. Trussov, Z. Bakenov and A. Mukanova, Polycationic doping of the LATP ceramic electrolyte for Li-ion batteries, *RSC Advances*, 2022, **12**, 29595-29601.
9. S. Hasegawa, N. Imanishi, T. Zhang, J. Xie, A. Hirano, Y. Takeda and O. Yamamoto, Study on lithium/air secondary batteries—Stability of NASICON-type lithium ion conducting glass–ceramics with water, *Journal of Power Sources*, 2009, **189**, 371-377.
10. V. Diez-Gómez, K. Arbi and J. Sanz, Modeling Ti/Ge Distribution in $LiTi_{2-x}Ge_x(PO_4)_3$ NASICON Series by ^{31}P MAS NMR and First-Principles DFT Calculations, *Journal of the American Chemical Society*, 2016, **138**, 9479-9486.
11. L. Zu-xiang, Y. Hui-jun, L. Shi-chun and T. Shun-bao, Phase relationship and electrical conductivity of $Li_{1+x}Ti_{2-x}Ga_xP_3O_{12}$ and $Li_{1+2x}Ti_{2-x}Mg_xP_3O_{12}$ systems, *Solid State Ionics*, 1986, **18-19**, 549-552.
12. H. Aono, E. Sugimoto, Y. Sadaaka, N. Imanaka and G. Adachi, Ionic conductivity of the lithium titanium phosphate $(Li_{1+x}M_xTi_{2-x}(PO_4)_3$ M= Al, Sc, Y, and La) systems, *Journal of the Electrochemical Society*, 1989, **136**, 590.
13. H. Aono, E. Sugimoto, Y. Sadaoka, N. Imanaka and G. y. Adachi, Ionic Conductivity of Solid Electrolytes Based on Lithium Titanium Phosphate, *Journal of The Electrochemical Society*, 1990, **137**, 1023.
14. K. Arbi, M. Tabellout, M. G. Lazarraga, J. M. Rojo and J. Sanz, Non-Arrhenius conductivity in the fast lithium conductor $L_{1.2}Ti_{1.8}Al_{0.2}(PO_4)_3$: A ^7Li NMR and electric impedance study, *Physical Review B*, 2005, **72**, 094302.
15. D. Rettenwander, A. Welzl, S. Pristat, F. Tietz, S. Taibl, G. J. Redhammer and J. Fleig, A microcontact impedance study on NASICON-type $Li_{1+x}Al_xTi_{2-x}(PO_4)_3$ ($0 \le x \le 0.5$) single crystals, *Journal of Materials Chemistry A*, 2016, **4**, 1506-1513.
16. H. Aono, E. Sugimoto, Y. Sadaoka, N. Imanaka and G.-y. Adachi, Electrical property and sinterability of $LiTi_2(PO_4)_3$ mixed with lithium salt (Li_3PO_4 or Li_3BO_3), *Solid State Ionics*, 1991, **47**, 257-264.
17. D. H. Kothari and D. K. Kanchan, Effect of doping of trivalent cations Ga^{3+}, Sc^{3+}, Y^{3+} in $Li_{1.3}Al_{0.3}Ti_{1.7}$ $(PO_4)_3$ (LATP) system on Li^+ ion conductivity, *Physica B: Condensed Matter*, 2016, **501**, 90-94.
18. L. Ladenstein, K. Hogrefe and H. M. R. Wilkening, Ionic Transport and Electrochemical Properties of NaSICON-Type $Li_{1+x}Hf_{2-x}Ga_x(PO_4)_3$ for All-Solid-State Lithium Batteries, *ACS Applied Energy Materials*, 2022, DOI: 10.1021/acsaem.2c01304.
19. T. Suzuki, K. Yoshida, K. Uematsu, T. Kodama, K. Toda, Z.-G. Ye, M. Ohashi and M. Sato, Structure refinement of lithium ion conductors $Li_3Sc_2(PO_4)_3$ and $Li_{3-2x}(Sc_{1-x}M_x)_2(PO_4)_3$ (M=Ti, Zr) with x=0.10 by neutron diffraction, *Solid State Ionics*, 1998, **113-115**, 89-96.
20. I. Y. Pinus, A. V. Khoroshilov, K. S. Gavrichev, V. P. Tarasov and A. B. Yaroslavtsev, On cationic mobility in Nasicon phosphates $LiTi_2(PO_4)_3$ and $L_{i0.9}Ti_{1.9}Nb_{0.1}(PO_4)_3$, *Solid State Ionics*, 2012, **212**, 112-116.
21. M. Cretin and P. Fabry, Comparative study of lithium ion conductors in the system $Li_{1+x}Al_xA_{2-x}^{IV}$ $(PO_4)_3$ with A^{IV}= Ti or Ge and 0≤x≤0·7 for use as Li^+ sensitive membranes, *Journal of the European Ceramic Society*, 1999, **19**, 2931-2940.
22. B. Nedjemeddine, The Origin of Phase Transition and the Usual Evolutions of the Unit-Cell Constants of the NASICON Structures of the Solid Solution $LiTi_{2-x}Ge_x(PO_4)_3$, *Physics of the Solid State*, 2019, **61**, 2446-2450.
23. E. A. Kurzina, I. A. Stenina, A. Dalvi and A. B. Yaroslavtsev, Synthesis and Ionic Conductivity of Lithium Titanium Phosphate-Based Solid Electrolytes, *Inorganic Materials*, 2021, **57**, 1035-1042.
24. S. Saffirio, M. Falco, G. B. Appetecchi, F. Smeacetto and C. Gerbaldi, $Li_{1.4}Al_{0.4}Ge_{0.4}Ti_{1.4}(PO_4)_3$ promising NASICON-structured glass-ceramic electrolyte for all-solid-state Li-based batteries: Unravelling the effect of diboron trioxide, *Journal of the European Ceramic Society*, 2022, **42**, 1023-1032.
25. A. Venkateswara Rao, V. Veeraiah, A. V. Prasada Rao, B. Kishore Babu and K. V. Kumar, Influence of Zr^{4+} doping on structural, spectroscopic and conductivity studies of lithium titanium phosphate, *Ceramics International*, 2014, **40**, 13911-13916.
26. A. Xu, R. Wang, M. Yao, J. Cao, M. Li, C. Yang, F. Liu and J. Ma, Electrochemical Properties of an Sn-Doped LATP Ceramic Electrolyte and Its Derived Sandwich-Structured Composite Solid Electrolyte, *Nanomaterials*, 2022, **12**, 2082.

27. H. Wang, H. Zhang, Y. Cheng, K. Feng, X. Li and H. Zhang, Rational design and synthesis of $LiTi_2(PO_4)_{3-x}F_x$ anode materials for high-performance aqueous lithium ion batteries, *Journal of Materials Chemistry A*, 2017, **5**, 593-599.
28. A. Kızılaslan, M. Kırkbınar, T. Cetinkaya and H. Akbulut, Sulfur doped $Li_{1.3}Al_{0.3}Ti_{1.7}(PO_4)_3$ solid electrolytes with enhanced ionic conductivity and a reduced activation energy barrier, *Physical Chemistry Chemical Physics*, 2020, **22**, 17221-17228.
29. J. B. Goodenough, H. Y. P. Hong and J. A. Kafalas, Fast Na^+-ion transport in skeleton structures, *Materials Research Bulletin*, 1976, **11**, 203-220.
30. X. Zhang, D. Butenko, L. Gao, X. Ye, B. Hong, S. Han, W. Xia, S. Wang, Y. Sun, Y. Zhao and J. Zhu, Synergistic Ion Diffusion in Lithium Titanium Phosphate Conductors: A Tale from Solo to Ensemble, *Chemistry of Materials*, 2023, **35**, 4541-4548.
31. K. Arbi, M. Hoelzel, A. Kuhn, F. García-Alvarado and J. Sanz, Local structure and lithium mobility in intercalated $Li_3Al_xTi_{2-x}(PO_4)_3$ NASICON type materials: a combined neutron diffraction and NMR study, *Physical Chemistry Chemical Physics*, 2014, **16**, 18397-18405.
32. K. Arbi, S. Mandal, J. M. Rojo and J. Sanz, Dependence of Ionic Conductivity on Composition of Fast Ionic Conductors $Li_{1+x}Ti_{2-x}Al_x(PO_4)_3$, $0 \le x \le 0.7$. A Parallel NMR and Electric Impedance Study, *Chemistry of Materials*, 2002, **14**, 1091-1097.
33. A. Aatiq, M. Ménétrier, L. Croguennec, E. Suard and C. Delmas, On the structure of $Li_3Ti_2(PO_4)_3$, *Journal of Materials Chemistry*, 2002, **12**, 2971-2978.
34. K. Arbi, A. Kuhn, J. Sanz and F. García-Alvarado, Characterization of Lithium Insertion into NASICON-Type $Li_{1+x}Ti_{2-x}Al_x(PO_4)_3$ and Its Electrochemical Behavior, *Journal of The Electrochemical Society*, 2010, **157**, A654.
35. R. Shannon, Revised effective ionic radii and systematic studies of interatomic distances in halides and chalcogenides, *Acta Crystallographica Section A*, 1976, **32**, 751-767.
36. D. A. Woodcock and P. Lightfoot, Comparison of the structural behaviour of the low thermal expansion NZP phases $MTi_2(PO_4)_3$ (M = Li, Na, K), *Journal of Materials Chemistry*, 1999, **9**, 2907-2911.
37. D. A. Woodcock, P. Lightfoot, D. A. Woodcock and C. Ritter, Mechanism of low thermal expansion in the cation-ordered Nasicon structure, *Chemical Communications*, 1998, DOI: 10.1039/A706928F, 107-108.
38. P. Lightfoot, D. A. Woodcock, J. D. Jorgensen and S. Short, Low thermal expansion materials: a comparison of the structural behaviour of $La_{0.33}Ti_2(PO_4)_3$, $Sr_{0.5}Ti_2(PO_4)_3$ and $NaTi_2(PO_4)_3$, *International Journal of Inorganic Materials*, 1999, **1**, 53-60.
39. D. Balaji and S. P. Kumar, $Bi_{0.33}Zr_2(PO_4)_3$, a negative thermal expansion material with a Nasicon-type structure, *Dalton Transactions*, 2022, **51**, 17310-17318.
40. S. J. L. Billinge, The rise of the X-ray atomic pair distribution function method: a series of fortunate events, *Philosophical Transactions of the Royal Society A: Mathematical, Physical and Engineering Sciences*, 2019, **377**, 20180413.
41. D. Keen, A comparison of various commonly used correlation functions for describing total scattering, *Journal of Applied Crystallography*, 2001, **34**, 172-177.
42. A. A. Coelho, P. A. Chater and A. Kern, Fast synthesis and refinement of the atomic pair distribution function, *Journal of Applied Crystallography*, 2015, **48**, 869-875.
43. Q. Ma, Q. Xu, C.-L. Tsai, F. Tietz and O. Guillon, A Novel Sol–Gel Method for Large-Scale Production of Nanopowders: Preparation of $Li_{1.5}Al_{0.5}Ti_{1.5}(PO_4)_3$ as an Example, *Journal of the American Ceramic Society*, 2016, **99**, 410-414.
44. P. J. Chupas, K. W. Chapman, C. Kurtz, J. C. Hanson, P. L. Lee and C. P. Grey, A versatile sample-environment cell for non-ambient X-ray scattering experiments, *Journal of Applied Crystallography*, 2008, **41**, 822-824.
45. B. H. Toby and R. B. Von Dreele, GSAS-II: the genesis of a modern open-source all purpose crystallography software package, *Journal of Applied Crystallography*, 2013, **46**, 544-549.
46. A. K. Soper, *GudrunN and GudrunX: programs for correcting raw neutron and X-ray diffraction data to differential scattering cross section*, Science & Technology Facilities Council, Swindon, UK, 2011.
47. E. Lorch, Neutron diffraction by germania, silica and radiation-damaged silica glasses, *Journal of Physics C: Solid State Physics*, 1969, **2**, 229.
48. Mantid Project, https://archive.mantidproject.org/Main_Page, (accessed 03/06/2024, 2024).
49. H. Rietveld, A profile refinement method for nuclear and magnetic structures, *Journal of Applied Crystallography*, 1969, **2**, 65-71.
50. A. A. Coelho, J. Evans, I. Evans, A. Kern and S. Parsons, The TOPAS symbolic computation system, *Powder Diffraction*, 2011, **26**, S22-S25.
51. G. J. Redhammer, D. Rettenwander, S. Pristat, E. Dashjav, C. M. N. Kumar, D. Topa and F. Tietz, A single crystal X-ray and powder neutron diffraction study on NASICON-type $Li_{1+x}Al_xTi_{2-x}(PO_4)_3$ ($0 \le x \le 0.5$) crystals: Implications on ionic conductivity, *Solid State Sciences*, 2016, **60**, 99-107.
52. M. Pogosova, I. Krasnikova, A. Sergeev, A. Zhugayevych and K. Stevenson, Correlating structure and transport properties in pristine and environmentally-aged superionic conductors based on $Li_{1.3}Al_{0.3}Ti_{1.7}(PO_4)_3$ ceramics, *Journal of Power Sources*, 2020, **448**, 227367.
53. G. W. Stinton and J. S. O. Evans, Parametric Rietveld refinement, *Journal of Applied Crystallography*, 2007, **40**, 87-95.
54. J. Liu, Z. Du, X. Wang, S. Tan, X. Wu, L. Geng, B. Song, P.-H. Chien, S. M. Everett and E. Hu, Anionic redox induced anomalous structural transition in Ni-rich cathodes, *Energy & Environmental Science*, 2021, **14**, 6441-6454.

55. B. J. Campbell, H. T. Stokes, D. E. Tanner and D. M. Hatch, ISODISPLACE: a web-based tool for exploring structural distortions, *Journal of Applied Crystallography*, 2006, **39**, 607-614.
56. H. T. Stokes, D. M. Hatch and B. J. Campbell, ISODISTORT, ISOTROPY Software Suite, https://stokes.byu.edu/iso/isodistort.php, (accessed 03/06/2024, 2024).
57. M. S. Chambers, D. S. Keeble, D. Fletcher, J. A. Hriljac and Z. Schnepp, Evolution of the Local Structure in the Sol–Gel Synthesis of Fe_3C Nanostructures, *Inorganic Chemistry*, 2021, **60**, 7062-7069.
58. J. S. O. Evans, Negative thermal expansion materials*Journal of the Chemical Society, Dalton Transactions*, 1999, DOI: 10.1039/A904297K, 3317-3326.
59. S. J. Hibble, A. M. Chippindale, E. Marelli, S. Kroeker, V. K. Michaelis, B. J. Greer, P. M. Aguiar, E. J. Bilbé, E. R. Barney and A. C. Hannon, Local and Average Structure in Zinc Cyanide: Toward an Understanding of the Atomistic Origin of Negative Thermal Expansion, *Journal of the American Chemical Society*, 2013, **135**, 16478-16489.
60. K. Arbi, M. Hoelzel, A. Kuhn, F. García-Alvarado and J. Sanz, Structural Factors That Enhance Lithium Mobility in Fast-Ion $Li_{1+x}Ti_{2-x}Al_x(PO_4)_3$ ($0 \leq x \leq 0.4$) Conductors Investigated by Neutron Diffraction in the Temperature Range 100–500 K, *Inorganic Chemistry*, 2013, **52**, 9290-9296.
61. M. Pérez-Estébanez, J. Isasi-Marín, D. M. Többens, A. Rivera-Calzada and C. León, A systematic study of Nasicon-type $Li_{1+x}M_xTi_{2-x}(PO_4)_3$ (M: Cr, Al, Fe) by neutron diffraction and impedance spectroscopy, *Solid State Ionics*, 2014, **266**, 1-8.
62. A. Mancini, J. F. Shin, A. Orera, P. R. Slater, C. Tealdi, Y. Ren, K. L. Page and L. Malavasi, Insight into the local structure of barium indate oxide-ion conductors: An X-ray total scattering study, *Dalton Transactions*, 2012, **41**, 50-53.
63. L. Puech, C. Cantau, P. Vinatier, G. Toussaint and P. Stevens, Elaboration and characterization of a free standing LiSICON membrane for aqueous lithium–air battery, *Journal of Power Sources*, 2012, **214**, 330-336.
64. A. Okuniewski, D. Rosiak, J. Chojnacki and B. Becker, Coordination polymers and molecular structures among complexes of mercury(II) halides with selected 1-benzoylthioureas, *Polyhedron*, 2015, **90**, 47-57.
65. V. Siller, A. Morata, M. N. Eroles, R. Arenal, J. C. Gonzalez-Rosillo, J. M. López del Amo and A. Tarancón, High performance LATP thin film electrolytes for all-solid-state microbattery applications, *Journal of Materials Chemistry A*, 2021, **9**, 17760-17769.
66. D. O. Semykina, O. A. Podgornova, S. B. Moodakare, R. Vedarajan and N. V. Kosova, Crystal Chemistry and Ionic Conductivity of the NASICON-Related Phases in the $Li_{3-x}Na_xV_2(PO_4)_3$ System, *Inorganic Chemistry*, 2023, DOI: 10.1021/acs.inorgchem.2c04351.